

**Superconducting Properties of $\text{Cu}_{0.5}\text{Tl}_{0.5}\text{Ba}_2\text{CaCu}_{2-x}\text{Ti}_x\text{O}_{8-\delta}$
($x=0, 0.5, 1, 1.5, 2$) Samples**



By

USAMA BIN IJAZ

**DEPARTMENT OF PHYSICS
QUAID-I-AZAM UNIVERSITY
ISLAMABAD, PAKISTAN**

2022

**Superconducting Properties of $\text{Cu}_{0.5}\text{Tl}_{0.5}\text{Ba}_2\text{CaCu}_{2-x}\text{Ti}_x\text{O}_{8-\delta}$
($x=0, 0.5, 1, 1.5, 2$) Samples**



*A dissertation submitted in partial fulfillment of the requirement for the
degree of Master of Philosophy in Physics*

by

Usama Bin Ijaz

**Materials Science Laboratory
Department of Physics
Quaid-i-Azam University
Islamabad, Pakistan**

2022



CERTIFICATE

To certify that Mr. Usama Bin Ijaz S/o Ijaz Ahmad Khan completed the experimental work for this dissertation under my supervision in the Materials Science Laboratory of the Physics Department at Quaid-i-Azam University Islamabad, satisfying the dissertation requirement for the degree of Master of Philosophy in Physics.

PA
A.8.125 Supervisor

Prof. Dr. Nawazish Ali Khan
Department of Physics
Quaid-i-Azam University
Islamabad, Pakistan

PA
19-8-2022
Submitted through:

Chairman

Prof. Dr. Nawazish Ali Khan
Department of Physics
Quaid-i-Azam University
Islamabad, Pakistan

**This thesis is dedicated to my parents.
For their endless love, support and
encouragement**

ACKNOWLEDGEMENT

I sincerely appreciate the almighty God for His graces, strength, sustenance and above all, His faithfulness and love from the beginning of my academic life up to this MPhil level. His benevolence has made me excel and successful in all my academic pursuits.

I would like to acknowledge and give my warmest thanks to my supervisor (Professor Dr. Nawazish Ali Khan) who made this work possible. His guidance and advice carried me through all the stages of writing my thesis. I would also like to thank my Lab-mates specially Ali Abbas and Madam Anila for letting my research work be an enjoyable moment, and for their brilliant comments and suggestions, thanks to them.

Finally, I would like to give special thanks to my parents and my younger brother (Umer Bin Ijaz) as a whole for their continuous support and understanding when undertaking my research and writing my thesis. Their prayer for me was what sustained me this far.



USAMA BIN IJAZ

Abstract

The solid-state reaction approach is used to create $\text{Cu}_{0.5}\text{Tl}_{0.5}\text{Ba}_2\text{CaCu}_{2-x}\text{Ti}_x\text{O}_{8-\delta}$ ($x=0, 0.5, 1, 1.5, 2.0$) superconductor samples, which are then examined using x-ray diffraction, resistivity, FTIR absorption and dielectric measurements. Orthorhombic crystals arrangement have shown by these samples in which unit cell volume (except for Ti-doping of $x=0.5$), suppresses as the Ti doping level increases in the final compound; in $\text{Cu}_{0.5}\text{Tl}_{0.5}\text{Ba}_2\text{CaCu}_{2-x}\text{Ti}_x\text{O}_{8-\delta}$ samples an antiferromagnetic order is most likely broken at the CuO_2 planar site that induces rise in the unit cell volume. The room temperature resistivity of $\text{Cu}_{0.5}\text{Tl}_{0.5}\text{Ba}_2\text{CaCu}_{2-x}\text{Ti}_x\text{O}_{8-\delta}$ ($x=0, 0.5, 1, 1.5, 2.0$) samples suppresses with rises in Ti-doping. These samples have displayed the zero resistivity critical at 99, 100.3, 100, 99.8, 100K and onset of superconductive characteristics around 111.3, 110.6, 112, 111.6, 109.5K respectively; which is the one of the remarkable feature of these samples is superconductivity at 100K in $\text{Cu}_{0.5}\text{Tl}_{0.5}\text{Ba}_2\text{CaTi}_2\text{O}_{8-\delta}$. Further conductivity analyses (FIC-analysis) of these samples' conductivity data have revealed that due to the lower density of mobile carriers at the $\text{CuO}_2/\text{TiO}_2$ planar sites, the parameter values such as $\xi_{c(0)}$, the Fermi velocity of superconducting carriers, the inter-layer coupling J , and the phase relaxation time of the carriers all decrease. The parameters value such as $B_{c(0)}$, $J_c(0)$ are slightly suppressed whereas the parameters values such as $\kappa=\lambda/\xi$ are rise showing reduced population of pinning centers in Ti-doped samples. Increased Ti-doping in the final molecule softens all of the absorption bands associated with the vibrations of different oxygen atoms in FTIR absorption tests. All of these oxygen atoms' vibrational modes are becoming softer, which is related to the Ti(47.9amu) atoms' lower mass as compared to Cu (63.546amu). The ac-conductivity of the dielectric constant increases in doped samples, revealing pronounced superconductivity in such samples, while the real part of the dielectric constant is suppressed in dielectric measurements while the imaginary part of it increases, showing more losses in Ti-doped samples.

Table of Contents

Chapter # 1	1
1 INTRODUCTION TO SUPERCONDUCTIVITY	1
1.1 Superconductivity:	1
1.2 Important characteristics of superconductors:	2
1.2.1 Zero Resistivity:	2
1.2.2 Perfect Diamagnetism/Meissner's Effect:	3
1.3 Superconducting state parameters:	4
1.3.1 Critical Temperature (T_c):	4
1.3.2 Critical Current Density (J_c):	5
1.3.3 Critical Magnetic Field (H_c):	5
1.3.4 Correlation between T_c , J_c and H_c :	6
1.4 Types of Superconductors:	7
1.4.1 Type-I Superconductors:	7
1.4.2 Type-II Superconductors:	8
1.5 Evolution of the theory of superconductivity:	9
1.5.1 London theory:	9
1.5.2 Ginzburg-Landau Theory:	12
1.5.3 B.C.S Theory:	13
1.6 ISOTOPE EFFECT:	14
1.7 FLUX QUANTIZATION:	15
1.8 Josephson Effect:	16
1.8.1 DC Josephson Effect:	16
1.8.2 AC Josephson Effect:	16
1.9 DIELECTRIC PROPERTIES OF SUPERCONDUCTOR:	16
1.9.1 Capacitor:	17
1.9.2 Dielectric Constants:	17
1.9.3 Dielectric Loss:	18
The ratio between the imaginary and real halves of the dielectric constant is known as tangent loss ' $\tan\delta$ '.	18
1.10 APPLICATIONS OF SUPERCONDUCTIVITY:	19
Chapter # 2	20

2	LITERATURE REVIEW	20
2.1	High Temperature Superconductors (HTSC):	20
2.2	Cu Tl Ba Ca Cu Ti O Series of Superconductors:	20
2.3	THALLIUM BASED HIGH TEMPERATURE SUPERCONDUCTORS:	21
2.3.1	Literature Review Of Thallium Based High Temperature Superconductors:	21
Chapter # 3		30
3	Experimental Methods	30
3.1	Sample preparation:	30
3.2	Characterization Methods:	30
3.2.1	X-Ray Diffraction (XRD):	31
3.2.2	ELECTRICAL RESISTIVITY MEASUREMENT (RT):	34
3.2.3	Fourier Transform Infrared Spectroscopy:	38
3.2.4	Dielectric measurements and ac conductivity:	41
3.2.5	Fluctuation induced conductivity analysis (FIC)	43
Chapter # 4		45
4	Results & Discussion	45
4.1	Introduction:	45
4.2	Experimental:	46
4.3	Result and Discussions:	48
4.3.1	X-ray Diffraction:	48
4.3.2	Resistivity Measurements:	50
4.3.3	FTIR Measurements:	54
4.3.4	$\text{Cu}_{0.5}\text{Tl}_{0.5}\text{Ba}_2\text{CaCu}_{2-x}\text{Ti}_x\text{O}_{8-\delta}$ (x=0, 0.5, 1, 1.5, 2.0) samples' excess conductivity analyses.	55
4.3.5	$\text{Cu}_{0.5}\text{Tl}_{0.5}\text{Ba}_2\text{CaCu}_{2-x}\text{Ti}_x\text{O}_{8-\delta}$ (x=0, 0.5, 1, 1.5, 2.0) samples' dielectric properties	62
4.4	Conclusions:	65

List of Figures

Figure 1.1: Resistivity versus temperature graph of mercury.....	1
Figure 1.2: Resistance VS Temperature curve for superconductor.	2
Figure 1.3: Meissner's effect in a material.....	3
Figure 1.4 Meissner effect.....	5
Figure 1.5 Critical magnetic fields as a function of temperature.....	6
Figure 1.6 Correlations between T_c , J_c and H_c	7
Figure 1.7 Type-I Superconductors.	7
Figure 1.8 Type-II Superconductors.	8
Figure 1.9 Penetration of magnetic field inside the superconductor.	12
Figure 1.10 Cooper pair formation in crystal lattice.	13
Figure 1.11 Capacitor.	17
Figure 1.12 Capacitance of a capacitor with and without dielectric material.	18
Figure 2.1 Capacitance of a capacitor with and without dielectric material.	21
Figure 3.1 Schematic diagram of X-ray diffraction through crystal	32
Figure 3.2 Working of XRD	33
Figure 3.3 The phonon contribution to the resistivity in normal metals.	35
Figure 3.4 Schematic of four-point probe	38
Figure 3.5: FTIR working.....	39
Figure 3.6 Schematic diagram of Michelson interferometer	40
Figure 3.7 Schematic diagram of FTIR apparatus.....	40
Figure 3.8 Experimental setup for dielectric properties	42
Figure 4.1 Shows the X-ray diffraction spectra of $Cu_{0.5}Ti_{0.5}Ba_2CaCu_{2-x}Ti_xO_{8-\delta}$ ($x=0, 0.5, 1, 1.5, 2.0$) samples.	49
Figure 4.2 The a and b-axis comparison of $Cu_{0.5}Ti_{0.5}Ba_2CaCu_{2-x}Ti_xO_{8-\delta}$ ($x=0, 0.5, 1, 1.5, 2.0$) samples with Ti-doping.....	49
Figure 4.3 The c-axis and volume comparison of $Cu_{0.5}Ti_{0.5}Ba_2CaCu_{2-x}Ti_xO_{8-\delta}$ ($x=0, 0.5, 1, 1.5, 2.0$) samples with Ti-doping	50
Figure 4.4 Resistivity versus temperature measurements of $Cu_{0.5}Ti_{0.5}Ba_2CaCu_{2-x}Ti_xO_{8-\delta}$ ($x=0, 0.5, 1, 1.5, 2.0$) samples	50
Figure 4.5 Resistivity versus temperature measurements of $Tl_{0.5}Ti_{0.5}Ba_2CaTi_2O_{8-\delta}$	52
Figure 4.6 Activation energy of $Tl_{0.5}Ti_{0.5}Ba_2CaTi_2O_{8-\delta}$	53
Figure 4.7 The FTIR absorption spectra of $Cu_{0.5}Ti_{0.5}Ba_2CaCu_{2-x}Ti_xO_{8-\delta}$ ($x=0, 0.5, 1, 1.5, 2.0$) samples.....	54
Figure 4.8 plot of $\ln\Delta\sigma$ and $\ln(\epsilon)$ of $Cu_{0.5}Ti_{0.5}Ba_2CaCu_{2-x}Ti_xO_{8-\delta}$ at $x=0$	55
Figure 4.9 plot of $\ln\Delta\sigma$ and $\ln(\epsilon)$ of $Cu_{0.5}Ti_{0.5}Ba_2CaCu_{2-x}Ti_xO_{8-\delta}$ at $x=0.5$	56
Figure 4.10 plot of $\ln\Delta\sigma$ and $\ln(\epsilon)$ of $Cu_{0.5}Ti_{0.5}Ba_2CaCu_{2-x}Ti_xO_{8-\delta}$ at $x=1$	56
Figure 4.11 plot of $\ln\Delta\sigma$ and $\ln(\epsilon)$ of $Cu_{0.5}Ti_{0.5}Ba_2CaCu_{2-x}Ti_xO_{8-\delta}$ at $x=1.5$	57
Figure 4.12 plot of $\ln\Delta\sigma$ and $\ln(\epsilon)$ of $Cu_{0.5}Ti_{0.5}Ba_2CaCu_{2-x}Ti_xO_{8-\delta}$ at $x=2$	57
Figure 4.13 Variation of Real part of dielectric constant with increase in Ti doping measured at frequency 100Hz and temperature 78K	63

Figure 4.14 Variation of Imaginary part of dielectric constant with increase in Ti doping measured at frequency 100Hz and temperature 78K.....	63
Figure 4.15 Variation of dielectric loss with increase in Ti doping measured at frequency 100Hz and temperature 78K	64
Figure 4.16 Variation of ac conductivity with increase in Ti doping measured at frequency 100Hz and temperature 80K	64

List of Tables

Table 1: Critical temperature of superconducting materials	4
Table 2 $T_c(R=0)$ and $T_c(\text{onset})$ temperatures of $\text{Cu}_{0.5}\text{Tl}_{0.5}\text{Ba}_2\text{CaCu}_{2-x}\text{Ti}_x\text{O}_{8-\delta}$ ($x=0, 0.5, 1, 1.5, 2.0$) samples.....	51
Table 3 Table of Superconducting parameters calculated from log plot of $\Delta\sigma$ and ϵ	60
Table 4 Table of Superconducting parameters calculated from FIC	62

Chapter # 1

1 INTRODUCTION TO SUPERCONDUCTIVITY

In this introductory section we will have a concise investigate the superconductors, a few theories to make sense of superconductivity, their properties and at last its applications.

1.1 Superconductivity:

Superconductivity is a phenomenon in which magnetic field lines are ejected out of some materials at low temperatures and the electric resistance of many materials completely disappears. On April 8, 1911, in Leiden, Heike Kimerling Onnes and one of his pupils made the discovery. (Simon & Smith, 1988)

The first instance of superconductivity was found in Mercury (Hg), whose resistivity quickly dissipated at 4K, meaning that at the critical temperature, the resistance instantly fell to zero.

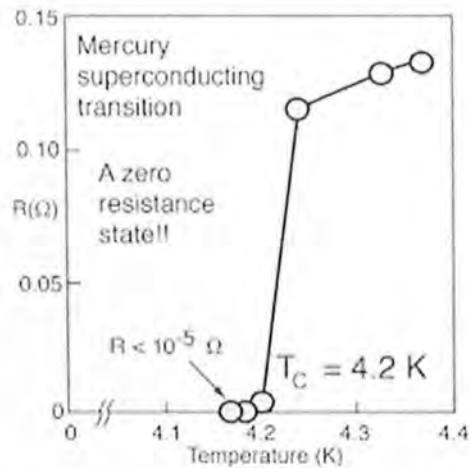


Figure 1.1: Resistivity versus temperature graph of mercury.

This marked a turning point in the development of electrical resistance and unlocked a new frontier for physics. As a phenomenon, superconductivity was described. Simply said, superconductivity is defined as the loss of all resistance at a specific temperature when the temperature of a material is dropped. Critical temperature is the temperature at which this phenomenon occurs.

1.2 Important characteristics of superconductors:

Superconductivity is a quantum mechanical phenomenon, and the superconducting state has two properties. (Fossheim & Sudbø, 2004) (i) Zero electrical resistance. (ii) Perfect diamagnetism/Meissner's Effect

1.2.1 Zero Resistivity:

Resistance is the term for the impediments to electron flow. In the normal state, electrons frequently collide with atoms, transferring their energy to the lattice atoms as a result. This causes the atoms to vibrate and release their energy as heat. As a result, energy continues to be lost. The definition of resistivity (Dunn et al., 1987)

$$\sigma = ne^2 \frac{\tau}{m} \quad (1.1)$$

$$\text{Where, } \rho = \frac{1}{\sigma}$$

$$\rho = \frac{m}{n\tau e^2} \quad (1.2)$$

Here, m stands for the mass of the electron, τ for mean free time, e for electron's charge, and n for electron number density. The sample is steadily cooled, and this causes the lattice vibrations to begin to freeze. The vibrations of the electron-lattice diminish as a result. Therefore, at a specific low temperature, the electrical resistance of superconductors totally vanishes for infinite mean free time. Cooper's pair is the name given to the pair of electrons that connect via phonons in the superconducting state. This cooper's pair can move without using excessive energy.

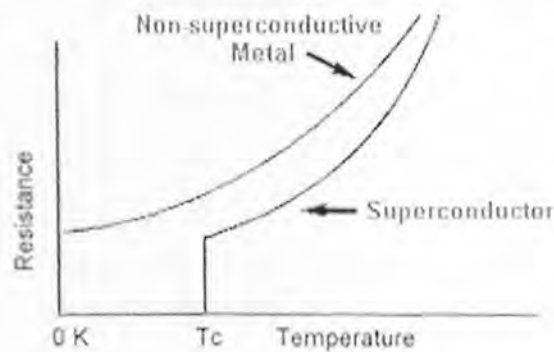


Figure 1.2: Resistance VS Temperature curve for superconductor.

1.2.2 Perfect Diamagnetism/Meissner's Effect:

As illustrated in Fig. 1.3, when diamagnetic materials are exposed to an external magnetic field, a magnetic field is induced and directed in the opposite direction in these materials, and the magnetic moments are aligned so as to repel the external field. Diamagnetism is the name for this phenomenon. (Isber et al., 2005)

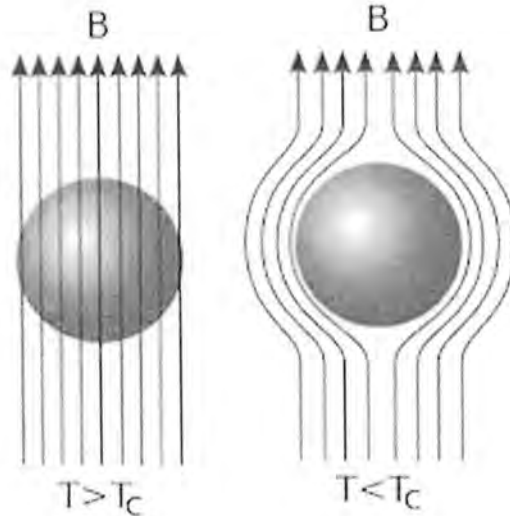


Figure 1.3: Meissner's effect in a material.

Meissner and Ochsenfeld discovered in 1933 that when superconductors are exposed to magnetic fields at $T < T_c$, the field is trapped inside the superconductor and will weaken as the temperature rises through T_c . The applied magnetic field has no bearing on this "frozen" magnetic field. The opposite phenomena is the Meissner's Effect.

Since,

$$B = \mu_o(H + M) \quad (1.3)$$

Magnetic field disappears in superconductors i.e. $B=0$

$$0 = \mu_o(H + M)$$

$$M = -H$$

Hence, the susceptibility is:

$$\frac{M}{H} = \chi = -1$$

$$\chi = -1 \quad (1.4)$$

This result demonstrates that superconductors have perfect diamagnetic behavior because it is the susceptibility of perfect diamagnetic material.

1.3 Superconducting state parameters:

The critical temperatures (T_c), critical current densities (J_c), and critical magnetic fields (H_c) are crucial for measuring superconductivity in a particular sample. These parameters must be below their critical values for a sample to exhibit superconducting characteristics.

1.3.1 Critical Temperature (T_c):

When a substance turns superconducting, its resistance is zero. Critical temperature is the range of temperature when this occurs. Reasonable resistivity occurs at the threshold temperature, but below it, the resistivity completely disappears. Below is a list of different superconductors' critical temperatures:

Materials	Critical temperature T_c (K)
Hg	4.6
Nb	9.3
C_6Ca	11.5
V_3Si	17.1
Nb_3Sn	18.3
$TlSrLaCuO_5$	40
$YBa_2Cu_3O_7$	90
$TlBa_2Ca_2Cu_3O_9$	120

Table 1: Critical temperature of superconducting materials

1.3.2 Critical Current Density (J_c):

Large currents are carried in thin superconducting wires because of their nearly zero resistance. However, there is a maximum current flow at which the sample loses its superconducting characteristics and returns to its regular condition. The critical current density is the highest current that can flow through per unit cross sectional area over which the sample exists in its normal state. In 1961, a researcher by the name of Kunzler made the first observation of J_c . Temperature affects critical current density. The critical current density value must exceed 1000 amperes per square millimetre (A/mm^2) in order to be used in practical applications. At very low temperatures, we can get up to 10^6 to 10^7 (A/cm^2) in superconductors based on thalium (5 K). (Mukuda et al., 2012) (Kunzler et al., 1961)

1.3.3 Critical Magnetic Field (H_c):

Superconducting materials will lose their superconducting condition when they are exposed to a strong magnetic field. i.e., they come back in their regular state. The Critical magnetic field H_c is the smallest field needed to eliminate superconductivity.

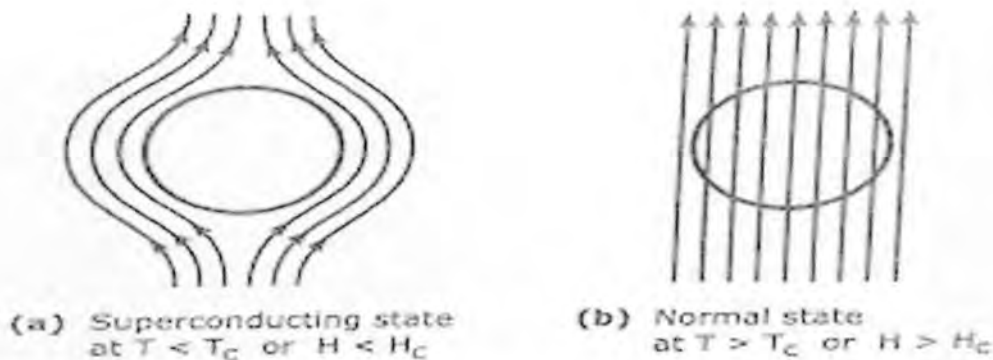


Figure 1.4 Meissner effect

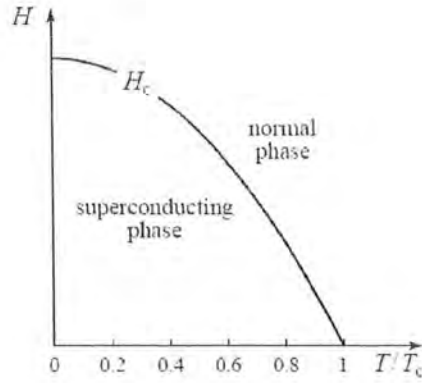


Figure 1.5 Critical magnetic fields as a function of temperature

Figure 1.5 demonstrates how "Hc" is dependent on temperature. When the temperature rises from T=0 K to T=Tc, it gets smaller. A relationship can be used to characterise the fluctuation of "Hc" ON "Tc" is given below.

$$H_c(T) = H_c(0) \left[1 - \left(T/T_c \right) \right] \quad (1.5)$$

At 0 K and T=TC, Hc (0) displays the highest value of the external magnetic field, and Hc (TC) is equal to 0. Additionally, the critical current value is

$$I_c = 2\pi H \quad (1.6)$$

1.3.4 Correlation between T_c, J_c and H_c:

The ability of a material to super-conduct depends on three crucial factors. These three factors are T_c, J_c and H_c. T_c is the critical temperature when there is no external magnetic field present and no current flowing. J_c is the critical current density at T=0K and H_c is the critical field strength when there is no current flowing. When these three critical values are taken into account, their plot creates a critical surface, and the material above this surface will be in a normal or mixed state.

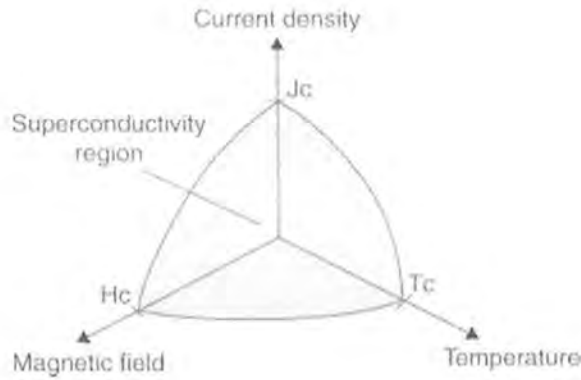


Figure 1.6 Correlations between T_c , J_c and H_c .

1.4 Types of Superconductors:

There are two types of superconductors, which can be distinguished by their magnetic properties. Initially, it was believed that all superconductors belonged to the same kind and that they all responded to an external magnetic field similarly. However, it was later found that there are various types of superconductors that respond to an external magnetic field differently. (Ginzburg & Landau, n.d.)

1.4.1 Type-I Superconductors:

Pure materials like metals, which are solely conductive in their usual form, make up Type I superconductors, which are typical superconductors. Type I superconductor's transition abruptly from the normal state to the superconducting state and have a low critical temperature. Because they can't withstand a strong magnetic field, Type I superconductors are often referred to as soft superconductors. Diamagnetism in Type I superconductors is flawless.

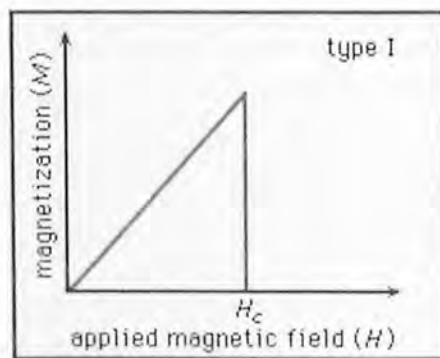


Figure 1.7 Type-I Superconductors.

1.4.2 Type-II Superconductors:

Hard superconductors, also known as type II superconductors, do not abruptly change from a normal state to a superconducting one. They might be transition metals or alloys. Figure shows that the material is in a perfect diamagnetic condition for region $H < H_{c1}$. The "lower critical field" is H_{c1} . The material enters a mixed state with mixed portions of normal and superconducting when the magnetic field is increased further. This mixed state, which ranges $H_{c1} < H < H_{c2}$, is also known as the material's vortex state. The material is said to be in its normal state when $H > H_{c2}$. (Schmidt, 1997)

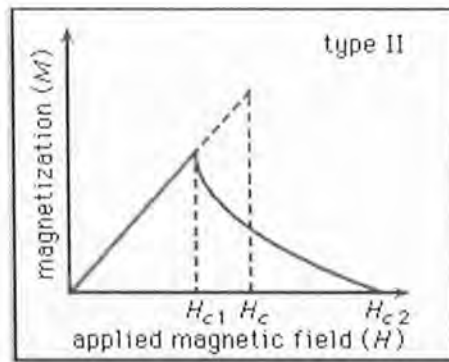


Figure 1.8 Type-II Superconductors.

1.4.2.1 SHUBNIKOV PHASE:

In 1937 superconductors exhibited an unusual behavior, according to L. V. Shubnikov and his coworkers. They discovered that vortices develop in some superconductors when an external magnetic field is present. Due to this, type-II superconductors were discovered, which likewise had a greater critical temperature than type-I superconductors.

This condition is also known as a vortex state. Instead of being entirely driven out of the material as is the case with type-I superconductors, the magnetic field lines remain inside the material when it transitions into the superconducting phase. As a result, the material is in a mixed or vortex state at this time, where the superconducting and normal states coexist. In 1957, A.A. Abrikosov gives a theoretical explanation of this phenomenon based on his experimental results. (A. A. ABRIKOSOV, 1964)

1.5 Evolution of the theory of superconductivity:

When superconductivity was discovered, numerous scientists began researching this fascinating phenomena and developing numerous ideas about it. The two-fluid model was first developed by C. J. Gorter and H. B. G. Casimir in 1934, and it was based on the idea that there were two different types of conducting electron fluid. They proposed that superconducting electrons are the cause of the behaviour of the superconducting state and that regular electrons are components of ordinary metals.

Heinz and Fritz London, two brothers, presented a phenomenological theory of superconductors for the first time in 1935. The foundation of London theory was the two fluid model. Later, another theory was put out by L.D. Landau and V.L. Ginzburg. The first quantum mechanical explanation for superconductivity was provided by their hypothesis. An order parameter was employed, which was the wave function " ψ ".

John Bardeen, Leon Neil Cooper, and John Robert Schrieffer developed the first microscopic theory of superconductivity, known as the BCS (**Bardeen-Cooper-Schrieffer**) theory, in 1957.

1.5.1 London theory:

Heinz and Fritz London developed a theory to explain the Meissner effect in 1935. They presented the idea of two types of electrons in the superconducting state: normal electrons (" n_n ") and superconducting electrons (" n_s "), with the overall density of electrons being given as $n = n_s + n_n$. The superconducting electrons dominate in the material as the temperature decreases to T_c ($T \rightarrow T_c$).

$$T \rightarrow T_c, n_n \rightarrow 0 \text{ so } n_s \rightarrow \text{max for } (T < T_c)$$

And,

$$T \rightarrow T_c, n_s \rightarrow 0 \text{ so } n_n \rightarrow \text{max for } (T > T_c)$$

Assuming that both fields are sufficiently faint to have no impact on the superconducting electrons, we may now apply a uniform electromagnetic field to the sample to make it superconducting. If we take V_s as the average velocity, m as the mass, and e as the charge of the super electron, then the equation of motion is

$$m (d v_s/d t) = -e E \quad (1.7)$$

And current density of the super electron is by:

$$J_s = -e n_s V_s \quad (1.8)$$

From questions 1.7 and 1.8 we get

$$dJ_s/dt = (n_s e^2/m) E \quad (1.9)$$

The first London equation is the one mentioned above. According to this equation, steady state current J_s flows at a constant rate in the absence of an electric field.

The current density of a normal electron is also known to be $J_n = \sigma E$. For $E=0$, $J_n=0$ which is the standard normal state behavior.

We will take into account the Maxwell equation for observing the magnetic behavior of the superconducting state.

$$\nabla \times E = - dB/d t \quad (1.10)$$

When $E=0$, B is constant, indicating that a homogenous magnetic field exists inside the superconducting material. However, this outcome runs counter to Meissner's effect theory.

London proposed some modification in the expression to remove this contradiction, the new equation is (**F. London and H. London, 1935**)

$$\nabla \times J_s = - \frac{n_s e^2 B}{m} \quad (1.11)$$

This equation, also referred to as London's second equation, supports the findings of the experiment.

1.5.1.1 Penetration Depth:

Only to a certain depth, known as the London penetration depth, magnetic field lines can penetrate into a superconductor when applied to the surface of the superconductor. It has an exponential decline and is indicated by the symbol λ_L .

From Maxwell's equation,

$$\nabla \times \mathbf{B} = \mu_0 \mathbf{J}_s \quad (1.12)$$

Use 1.11 and taking curl of 1.12, we get

$$\nabla \times (\nabla \times \mathbf{B}) = -\frac{\mu_0 n_s e^2 B}{m} = \frac{-1}{\lambda^2} B \quad (1.13)$$

Taking

$$\lambda_L = (m_e / \mu_0 n_s e^2)^{1/2}$$

This shows the London penetration depth.

Since,

$$\nabla \times (\nabla \times \mathbf{B}) = \nabla (\nabla \cdot \mathbf{B}) - \nabla^2 \mathbf{B}$$

And we also know

$$(\nabla \cdot \mathbf{B}) = 0$$

So, equation 1.12 will become

$$\nabla^2 \mathbf{B} = \frac{1}{\lambda^2} \mathbf{B}$$

For x-component

$$B = B_0 e^{-x/\lambda_L} \quad (1.14)$$

In this case, \mathbf{B}_0 is the external magnetic field and the value of λ_L has a range between 50nm

to 500nm.

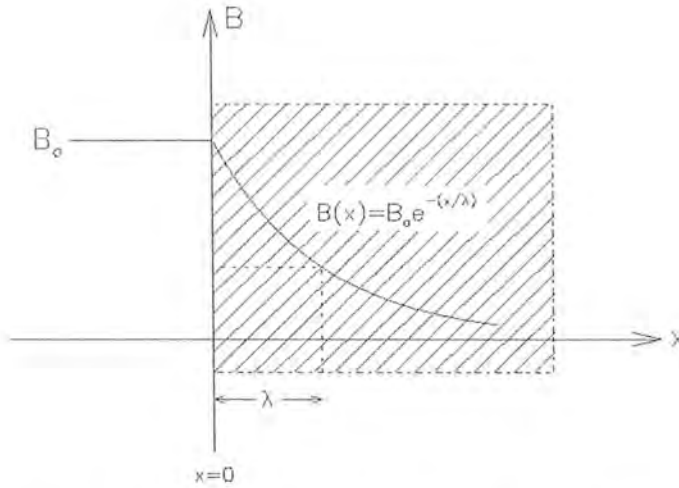


Figure 1.9 Penetration of magnetic field inside the superconductor.

The temperature also affects the depth of London penetration. It diminishes as the temperature rises, and its expression is shown. (Schmidt, 1997)

$$\lambda(T) = \lambda_0 \left[1 - \left(\frac{T}{T_c} \right)^2 \right]^{-1/2} \quad (1.15)$$

Where λ_0 is the penetration depth when temperature is zero kelvin.

1.5.2 Ginzburg-Landau Theory:

In 1950, V.L. Ginzburg and L.D. Landau proposed the GL theory, which is regarded as the first quantum mechanical explanation of superconductivity. Due to the second order phase shift from the normal to the superconducting state, the wave function was used in the GL theory rather than the London theory, which ignored all quantum mechanical effects. They introduced the concept of an order parameter (Mandal et al., 1990) and proposed that this order parameter has a zero value in the normal state and a finite non-zero value in the superconducting state, i.e.

$$\Psi(T) = 0; \text{ If } T > T_c$$

$$\Psi(T) \neq 0; \text{ If } T < T_c$$

So, in accordance with GL theory, the order parameter provides information on the system's state.

According to GL theory, Ψ is a superconductor's macroscopic wave function and should be a complex number. The normalized order parameter was used in the construction of this theory.

$$|\psi|^2 = \frac{n_s}{2}$$

Where n_s is the number density of the superconducting electrons.

1.5.3 B.C.S Theory:

Three physicists, Bardeen, Cooper, and Schrieffer, developed the BCS theory in 1957 to explain the idea of superconductivity using cutting-edge quantum mechanical notions. According to BCS theory, the creation of cooper pairs causes the microscopic phenomena of superconductivity. (Bardeen et al., 1957)

1.5.3.1 Formation of Cooper Pairs:

According to BCS theory, when electrons move through a lattice of positive ions, they cause deformation.

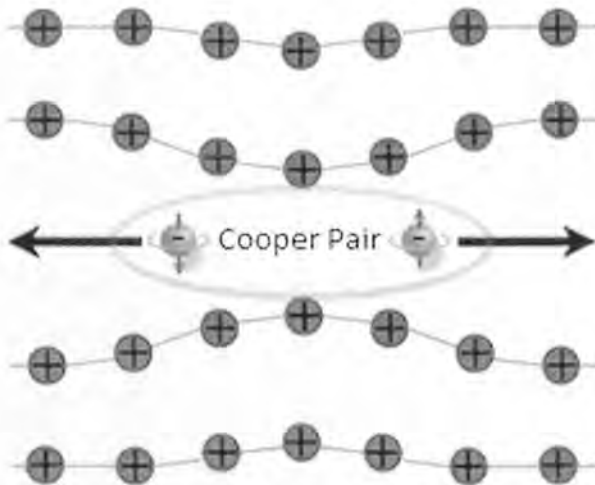


Figure 1.10 Cooper pair formation in crystal lattice.

Hence, atoms of lattice vibrate and these vibrations are known as phonons. An electron in a metal can move around freely, repelling other electrons with similar charges, but they also attract

ions, which causes the lattice to deform. In order to produce a positive ion core, ions must attract an electron and give it additional positive charge. Other electrons with the opposite momentum and spin are drawn to this stronger positively charged ion core. (Ibach & Lüth, 2009) Despite being fermions like electrons, their total spin is zero like bosons. There may be several Cooper pairings in one state. This electron pair is referred to as the Cooper pair. The primary cause of superconductivity is the Cooper pair.

1.5.3.2 Coherence Length (ξ):

The closeness of the electrons in a cooper pair is not necessary. They may be far apart because of how wide their interaction extends. Coherence length is the distance between the two electrons in a cooper pair. (S. O.. Pillai, 2018) It has a varied value for high- and low-temperature superconductors; for high- and low-temperature superconductors, it has a small and large value, respectively. The coherence length for superconductivity derives from BCS theory.

$$\xi = \frac{\hbar V_F}{2\Delta}$$

Where 2Δ is the energy gap and V_F is the Fermi velocity.

For Type I superconductors: $\xi > \lambda_L$

For Type II superconductors: $\xi < \lambda_L$

1.6 ISOTOPE EFFECT:

It was discovered in 1950 that the critical temperature of an element varies depending on the isotope, and that this temperature is inversely proportional to isotope mass (Conder, 2001) i.e.

$$T_c M_\alpha = \text{constant} \tag{1.36}$$

Where $\alpha = 0.5$

The critical temperature for several mercury isotopes was found to be:

$$\text{Hg}(199.5\text{amu}) = 4.185 \text{ K}$$

$$\text{Hg}(203.4\text{amu}) = 4.146 \text{ K}$$

1.7 FLUX QUANTIZATION:

The existence of magnetic flux quantization was discovered in 1961. It was almost simultaneously found separately by scientists in Germany and the USA.

Consider a superconducting loop that is initially at a temperature $T > T_c$ and is exposed to an external magnetic field in order to comprehend the phrase flux quantization. The field lines relevant to the Meisner effect are pushed out of the material when the temperature of this loop is reduced until it falls below the critical temperature. The flux that has been caught in the loop is still there, even if the external field is cut off. Due to the faradays law of induction, the magnetic flux through the loop first declines when the external field is removed. However, because the loop is now in a superconducting condition, the currents continue to flow without interruption and the loop begins to maintain the flux. The current would have decreased and the flux would have degraded if the ring had any resistance, but because the flux takes an indefinite amount of time to degrade in this situation, it appeared to be locked in a loop.

The magnetic field multiplied by the loop's area is known as magnetic flux i.e. $\Phi = B \cdot A$. However, when discussing a superconducting loop, the flux Φ that passes through the loop is always quantized. It implies that there are limits to the flux's possible values. This expression's equation is:

$$\Phi = \frac{2ne}{e^*} \Phi_0 \quad (1.17)$$

Here Φ is the total flux confined in a hole and Φ_0 is flux quantum having value $\frac{hc}{2e} = 2.0679 \text{ G cm}^2$ and $e^* = 2e$ (corresponding to cooper pair).

The opposite of the flux quantum is defined as the Josephson constant and this is constant of proportionality in Josephson Effect:

$$C_j = 1/ \Phi_0 \quad (1.18)$$

1.8 Josephson Effect:

Barian David Josephson predicted that super-current flows across the Josephson junction in 1962. He said that it was a macroscopic quantum mechanical tunneling process. He explained that cooper pairs tunneling across the Josephson junction allow current to pass through a tiny insulating barrier between two superconductors (Josephson junction) (**Josephson, 1962**). The Josephson Effect is the term used to describe this tunneling of cooper pairs over the junction.

Types of Josephson Effect:

There are two types of Josephson Effect.

1.8.1 DC Josephson Effect:

Without the application of any external voltage, a DC current moves through an insulator in this occurrence. Cooper pair's flow is known as a super-current, as we all know. Without any external voltage, it continues to flow. Josephson was the first scientist to postulate that the flow of current through an insulator positioned between two superconductors was caused by the phenomena of quantum tunneling. The insulating layer can be passed through by cooper pairs. The particles just don't notice the insulating layer's presence and readily pass through the barrier. This phenomenon is known as DC Josephson effect. (**Tafuri, 2019**)

1.8.2 AC Josephson Effect:

A fixed DC voltage is put across the junction's ends to create the AC Josephson effect, which causes a sinusoidal current to flow through the junction with linearly increasing phase over time. As a voltage to frequency converter, the AC Josephson junction can be said to function. (**Tafuri, 2019**)

1.9 DIELECTRIC PROPERTIES OF SUPERCONDUCTOR:

We examine the dielectric property of permittivity in superconducting samples. Permittivity is known to be changeable and to fluctuate with changes in temperature, frequency, pressure, and sample structure.

1.9.1 Capacitor:

The device known as a capacitor is used to store charge in an electric field. A dielectric material is sandwiched between two conducting plates to create capacitors. Silver paste is painted on both sides of the sample to create a capacitor made of a superconductor.

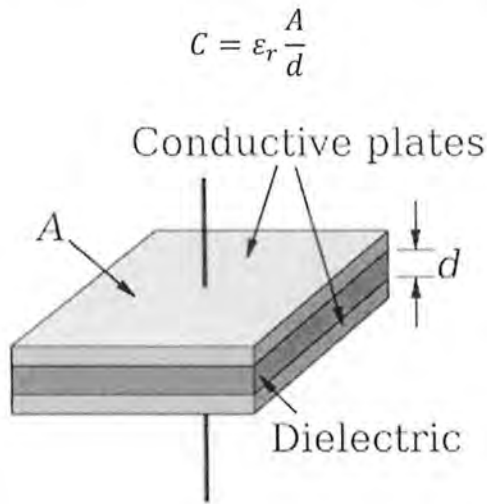


Figure 1.11 Capacitor.

1.9.2 Dielectric Constants:

When an electric field is applied, a dielectric material has the capacity to store energy. When a voltage is supplied across a capacitor's plates, charging begins. In comparison to when no material is inserted between the plates, a dielectric substance placed there increases the capacity of the device to store charges. Therefore, by adding dielectric material between a capacitor's plates, its ability to store charges is boosted. The complicated quantity known as the dielectric constant is connected to the capacitance of a capacitor made of dielectric material

$$C = \epsilon_o \frac{A}{d} \quad C = \epsilon_r \frac{A}{d}$$

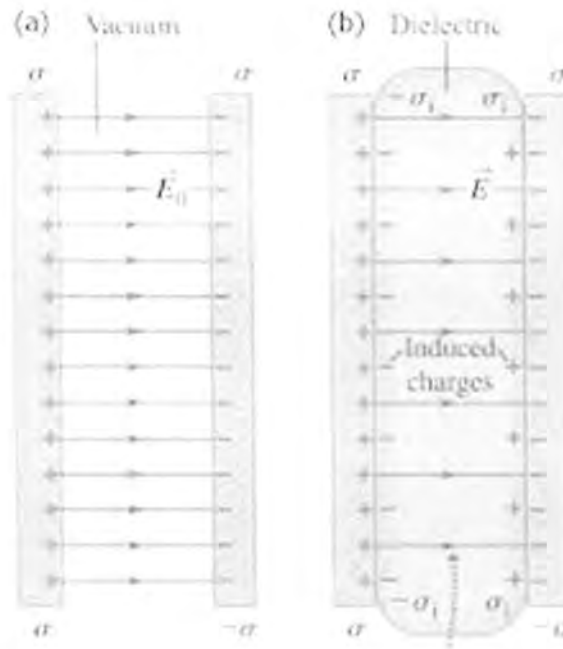


Figure 1.12 Capacitance of a capacitor with and without dielectric material.

Area is represented by A , the separation between the plates is represented by d , and the dielectric constant is represented by ϵ also known as permittivity of a material.

Since the dielectric constant (ϵ) is a complicated quantity, its real part (ϵ_r') indicates how much energy is actually held in a substance. Its loss factor, represented by the imaginary component (ϵ_r''), demonstrates how susceptible a material is to an external electric field. Although (ϵ_r'') is typically much less than (ϵ_r'), it is always more than zero and (ϵ_r'') has the characteristics of both conductivity and dielectric loss.

1.9.3 Dielectric Loss:

The ratio between the imaginary and real halves of the dielectric constant is known as tangent loss ' $\tan\delta$ '.

$$\text{Tan}\delta = \epsilon_r'' / \epsilon_r' \quad (1.19)$$

It is also known as the dissipation factor or $\tan\delta$.

1.10 APPLICATIONS OF SUPERCONDUCTIVITY:

The following are some potential uses for superconductivity:

1. Superconducting quantum interference devices, or SQUIDS, are instruments that track exceedingly weak magnetic fields. It can be utilized to build the most sensitive magnetometers and as sensors.
2. In experimental plasma physics, the confinement of plasma requires very strong magnetic fields. It is common practice to create such strong magnetic fields using superconductors.
3. Superconductors can produce strong magnets for magnetic levitation trains in the transportation industry.
4. The huge hadron collider can also be utilized to accelerate particles thanks to the strong magnetic fields produced by superconductors.
5. Magnetic resonance imaging can utilize superconductors in the medical field.
6. High-speed computers will soon be powered by superconductors.
7. Satellites can be sent into orbit without the use of rockets by using magnetic propulsion.

Chapter # 2

2 LITERATURE REVIEW

In this chapter, i will give a short overview of High Temperature Superconductors (HTSC), Thallium (TI) based High Temperature Superconductors (HTSC), some simple CuTI superconductor's structures and Ti doped TI-based HTSC.

2.1 High Temperature Superconductors (HTSC):

In general, empirical elements have very low transition temperatures. At very high temperatures, alloys like Nb-Ti and Nb-Al-Ge change. Oxide superconductors with T_c of 90–125K were found in 1986 by Bednorz and Muller. Following this discovery, Paul Chu and his colleagues found 123 $\text{XBa}_2\text{Cu}_3\text{O}_{7-x}$ -type oxides with T_c about 90K. The discovery of superconductors with T_c higher than liquid nitrogen temperature encouraged scientists to launch an extensive search for other oxides with higher T_c . Compounds from the Bi-Sr-Ca-Cu-O and TI-Ba-Ca-Cu-O families have been found to have T_c values between 60K and 125K.

2.2 Cu TI Ba Ca Cu Ti O Series of Superconductors:

$\text{Cu}_{0.5}\text{TI}_{0.5}\text{Ba}_2\text{CaCu}_{2-x}\text{Ti}_x\text{O}_{8-6}$ is this family's most crucial member (1212). It comprises two charge reservoir layers and two layers of copper oxide planes in between. These superconductors have a tetragonal system with the space group $P4mmm$ (Hassan & Khan, 2008). Superconductors made of CuTI-1212 can be employed in bulk as well as thin films, making them readily applicable in real-world settings.

Only the $x = 2$ and $x = 3$ structures in this class of compounds have had their details improved using single-crystal x-ray diffraction data. Here the unit cells of the TIO monolayer compounds are structurally primitive tetragonal $P4/mmm$. As a result, there is no body-centered symmetry and the single TIO layer is absolutely flat. Pyramids contain significant anisotropies Cu-O bond length, comparable to those in the TIO double-layer compounds. Pyramidal CuO layers appear to have a covalent nature in this system as well. The TIO monolayer system relaxes the dimensional mismatch by dislodging TI atoms from their ideal locations, in contrast to the oxygen displacements in TIO double-layer complexes.

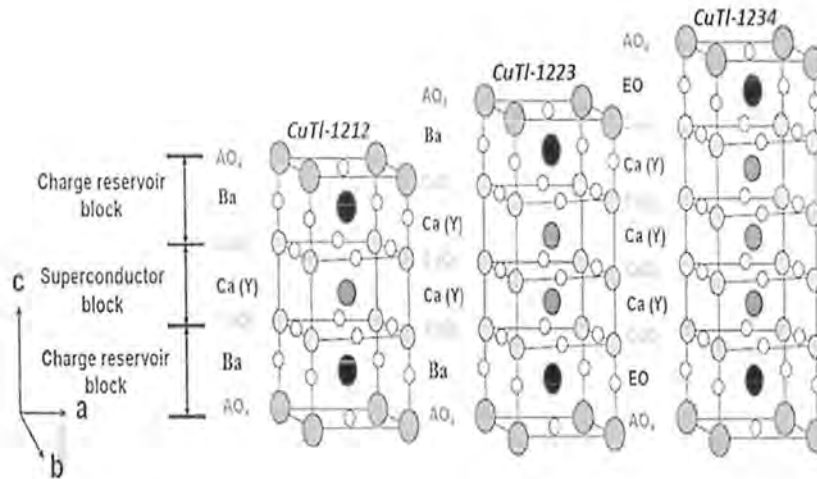


Figure 2.1 Capacitance of a capacitor with and without dielectric material.

2.3 THALLIUM BASED HIGH TEMPERATURE SUPERCONDUCTORS:

Tl-Ba-Ca-Cu-O superconductors are regarded as the best superconductors because of their high T_c . This superconductor family has a high critical current density and a low microwave surface resistance. This series was first uncovered in 1988 by Sheng and Hermann (**Hazen et al., 1988**). The crystal structure of these superconductors is mostly tetragonal, with alternating single or dual Tl-O sheets and Tl-Ba-Ca-Cu-O layers that resemble perovskites (Parkin, Lee, Nazzari, et al., 1988). crystal structure of a superconductor from the (CuTl)-Ba-Ca-Cu-O family.

2.3.1 Literature Review Of Thallium Based High Temperature Superconductors:

In 1988, Z. Z. Sheng made the initial discovery of the Tl-Ba-Cu-O family of thallium-based superconductors (**Sheng & Hermann, 1988**). This family showed a zero-resistance critical temperature $T_c(R=0)$ above 90 K, showing that other elements can be added to raise the $T_c(R=0)$ above the parent compound. Additionally, they found that adding Ba at the Ca site causes $T_c(R=0)$ to increase above 100 K and leads to an onset temperature of 120 K. They contend that the superconductor they discovered is stronger and more reliable.

Parkin discovered the zero resistance critical temperature for $Tl_2Ba_2Ca_2Cu_2O_{8.8}$ superconductors between 118K and 127K(**Parkin, Lee, Engler, et al., 1988**). They found that T_c fluctuates as a result of environmental factors and is reliant on those factors. Transmission electron spectroscopy allowed the body-centered tetragonal shape of the $Tl_2Ba_2Ca_2Cu_2O_{8.8}$ unit cell to be identified.

Under extreme pressure of up to 21GPa, D. Tristron developed $Tl_2Ba_2Ca_2Cu_3O_{10+x}$ and $Tl_2Ba_2Ca_3Cu_4O_{12+x}$ samples. They measured resistivity using a four-probe method. This four probe approach was created by Van Eenige for use in high-pressure experiments. At atmospheric pressure, their respective critical temperatures are 128.5 K and 113 K, but as the pressure was increased, these temperatures increased to 133 K for one sample and 120 K for the other. (**Jover et al., 1993**)

With excellent results, H. Ihara created a single-layered thallium oxide superconductor with the formula $Tl Ba_2 Ca_{n-1} Cu_n O_y$ ($n = 3$ and 4) (**Ihara et al., 2000**). Single-layered TlO superconductors are more difficult to synthesize and have more unstable phases than double-layered superconductors, but from an application standpoint they are more effective due to their higher critical temperature and current density. They utilize Sr at the Ca site and Pb or Bi at the Tl site to prevent phase instability. They contend that the main obstacle to the creation of the $Tl Ba_2 Ca_{n-1} Cu_n O_y$ ($n = 3$ and 4) phases is the presence of carbon impurities.

Without any element replacement, E. Ohshima achieved single phase $TlSr_2Ca_2Cu_3O_x$ by applying 2.5GPa pressure to $TlSr_2Ca_2Cu_3O_x$. Using SQUID, the sample was synthesized at 10,000°C for 4 hours, and $T_c=97K$ was recorded (**Ohshima et al., 1997**). They found that their sample had a tetragonal structure using the XRD technique. They found that Tl escapes during the synthesis of $TlSr_2Ca_2Cu_3O_x$, forming a long-ordered structural instability, and does not evaporate at air pressure.

In their $(Cu_{0.5} Tl_{0.5}) Ba_2Ca_2Cu_3O_x$ (CuTl 1223) samples, K. Tokiwa asserted that at room temperature $T_c=130$ K (**Tanaka et al., 2001**). They then evaluated the effect on T_c in a cubic anvil cell under 8 GPa pressure. The XRD technique was used to examine the crystallinity of CuTl 1223. When measuring resistivity with a four-probe setup, they discovered that the onset temperature increased from 134.6 K to 147.0 K at 8 GPa of pressure.

Bulk $Cu_{0.5}Tl_{0.5}Ba_2Ca_2Cu_3O_x$ was created by N.A. Khan using the solid state reaction technique (**Khan et al., 2005**). $Cu(CN)$, $Ba(NO_3)_2$, and $CaCO_3$ were ground using a mortar and pestle, and the mixture was then burned at 840°C. Then, after fire, TlO_3 was added to the mixture, and pallets were created. These pallets were sintered for 30 minutes while covered in aluminum foil.

They detected $T_c(R=0)$ at 103K and T_c^{onset} at 110K utilizing the four probe approach. They were able to verify that the sample was optimally doped by FTIR tests.

The idea of substituting Ca with Mg and Be in different ratios in $\text{Cu}_{0.5}\text{Tl}_{0.5}\text{Ba}_2\text{Ca}_2\text{Cu}_3\text{O}_{10-\delta}$ was first proposed by N.A. Khan (**Khan & Khurram, 2005**) & (**Khan & Husnain, 2006**). These samples were created using $\text{Cu}(\text{CN})$, $\text{Ba}(\text{NO}_3)_2$, MgO , and $\text{Ca}(\text{NO}_3)_2$. These samples were milled for exactly one hour and then burned in quart-sized boats at 8400 degrees. After the first firing, they ground the mixture once more and put it in the furnace for a second firing at the same temperature. The final product, $\text{Cu}_{0.5}\text{Tl}_{0.5}\text{Ba}_2\text{Ca}_{2-x}\text{Mg}_x\text{Cu}_3\text{O}_{10-\delta}$, is created by mixing Tl_2O_3 last by grinding, where ($x=0,0.5,1,1.5$). The finished product was palletized, covered in aluminum foil, and sintered for ten minutes. They saw a consistent pattern of increased T_c in response to different Ca doping levels. Using four probe resistivity tests, they found that $T_c(R=0)$ is 82K for $x=0$ composition and 92K for $x=1.5$ composition. They concluded from their research that an increase in $T_c(R=0)$ results from doping a less electronegative Ca site with more electronegative Mg, which drives Cu electron clouds in Mg's direction. It might be the cause of the c-axis length drop that an XRD analysis can detect. Additionally, they carried out FTIR studies, which revealed the apical modes' softening to lower wave numbers.

$\text{Cu}_{0.5}\text{Tl}_{0.5}\text{Ba}_2\text{Ca}_2\text{Zn}_x\text{Cu}_{3-x}\text{O}_{10-\delta}$ ($x = 0.75, 1.5, 2.25, 2.65$) samples were produced by N. A. Khan (**Khan & Mumtaz, 2006**) using a two-step solid-state reaction technique, and he discovered that substituting Zn at the Cu planar site enhanced superconducting characteristics. Due to the replacement of Zn in different ratios, the XRD examination revealed a tetragonal shape and a reduction in c axis length. Rising order in resistivity was seen as a function of Zn substitution concentration using four probe resistivity measurements. The highest T_c recorded is 121 K for $x=2.65$. Ac susceptibility tests, which demonstrate a developing pattern of rising Zn content, were used to confirm the existence of the bulk diamagnetic state. The results of an FTIR investigation of various Zn concentrations show that Zn behaves the same in planar oxygen modes while the apical oxygen phonon modes soften to a lower wave number.

Superconductors $\text{Tl}_2\text{CaBa}_2\text{Cu}_2\text{O}_8$ (2122) and $\text{Tl}_2\text{Ca}_2\text{Ba}_2\text{Cu}_3\text{O}_{10}$ (2223) were made utilizing a modified powder synthesis method created by N. L. Wu (**Wu et al., 1989**). They prepared Tl_2O_3 , CuO , and $\text{CaBa}_2\text{CuO}_4$ in a stoichiometric combination for both samples, but for sample 2223, they added CaO and CuO as an extra reactant to meet the stoichiometry requirements. After

claiming sample 2122 at 830°C for 14 hours, the critical temperature T_c ($R = 0$) was determined using a four-probe system. T_c ($R=0$) turned out to be 116 K. According to their XRD analysis, their sample produced a single phase with few contaminants. To create the single method with the fewest contaminants, they calcined the 2223 sample twice. The first stage of calcination lasted for five hours at 830°C, while the second stage lasted for two to six hours at 870°C. They used four probe techniques to find T_c ($R = 0$) between 110 and 118 K. Both of their samples displayed an abrupt change and a 20% saturated Meissner effect when subjected to a 20 G magnetic field. Powder melting, which results in significant thallium loss during calcination and the buildup of impurities that don't behave like superconductors, is the process's main flaw.

Carbon nanotubes were doped in a CuTl-1223 superconductor by M. Rafique at various weight percentages (0 to 7 wt. percent) (**Rafique et al., 2014**). A two-step solid state reaction technique was employed for the synthesis of their samples. To categorize their sample, they used XRD, a resistivity device with four probes, and scanning electron microscopy. Their sample has an orthorhombic structure with one phase, as determined by XRD analysis. The c axis length varied only slightly between Carbon atom intercalation from carbon nanotubes in the unit cell may be the cause of the range of 0.27 to 0.20. Through carbon nanotubes, which enhance intergranular current flow, their sample's SEM investigation demonstrated inter-grain linkage. The 3D regime has contracted and superconducting characteristics including coherence volume, fermi velocity, and binding constant have been inhibited as the concentration of carbon nanotubes has risen, according to a study on fluctuation-induced conductivity (FIC). They provide an explanation for the diffusion of carbon atoms from carbon nanotubes into the unit cell, which suppressed the superconducting parameter by functioning as a columnar defect of a non-superconducting existence.

Y. Shimakawa developed samples of $Tl_2Ba_2CaO_6$. In their superconducting samples, they investigated the crystal structure, critical temperature (T_c), and carrier concentration (**Shimakawa et al., 1989**). They hypothesized that the critical temperature (T_c) value of their samples is connected to the length of the c axis; they also claimed that variations in the oxygen content were to blame for variations in the transition temperature. They demonstrated how carrier concentration affects transition temperature (T_c). They also realized that by adding 0.1 percent more oxygen per formula, the critical temperature (T_c) may rise to around 80 K and the

length of the c-axis might increase by 0.4%. They claimed that increasing the amount of dopant would cause the critical temperature T_c to drop. They came to the conclusion that in their samples, increasing the concentration of holes inhibited the superconducting while decreasing the concentration of holes promoted the superconductivity. They explained how the transition temperature varied as the number of sheets of CuO_2 per unit formula increased. The number of concentration carriers per sheet decreased as they raised it (CuO_2). They pointed out that superconductivity only exists within a certain acceptable range of carrier concentration.

$\text{Bi}_{1.84}\text{Pb}_{0.34}\text{Sr}_{1.91}\text{Ca}_{2.03}\text{Cu}_{3.06}\text{In}_x\text{O}_y$ superconductors doped with indium were the subject of research by R. K. Nkum (**Nkum et al., 2002**). They investigated the behavior of resistivity using the four probe approach. For measuring the samples' dielectric properties, they employed a Wayne Kerr optical LCR meter. The usual solid state reaction procedure was used to make the samples, which were then palletized. They noticed that as indium's concentration grew, the dielectric constant likewise did so, resulting in an improvement in the sample's polarization. By raising Indium concentration, loss tangent was reduced. Increased resistivity results from a decrease in carrier concentration, which may be brought on by localization of the charge carriers and magnetic anomalies in the CuO_2 plane.

The dielectric characteristics of $\text{Tl}_2\text{Ba}_2\text{Ca}_2\text{Cu}_3\text{O}_x$ (Tl2223) and $\text{Tl}_2\text{Ba}_2\text{CaCu}_2\text{O}_x$ were investigated by S. Cavadar (Tl2212) (**Çavdar et al., 2005**). Pallets of synthetic samples were used as their samples. The samples' dielectric properties were then examined using an impedance analyzer, four-probe resistivity tests, and XRD for the structural investigation. T_{conset} was observed at 125K, and T_{offset} at 112K. The sample must have had two stages because there was almost a 13-point difference between T_{offset} and T_{conset} , which was supported by XRD patterns. All real and imaginary constants, tan losses, and ac conductivities of the samples were measured during dielectric measurements. They looked at how changes in frequency and temperature affect the behavior of negative capacitance, dielectric constants, tan loss, and conductivity. They keep the frequency between 7 KHz and 2 MHz while observing that the actual change was brought on by a change in temperature. Dipolar polarization has increased, which is the cause of the rising behavior. They discovered that there is little change in the dielectric constants at higher frequencies (2- 10 MHz). Although the imaginary portion of the dielectric constant exhibited an increasing behavior with decreasing frequency and temperature, it has a lesser dispersion than

the actual portion. Tan losses exhibited little change at higher frequencies, although they did indicate a dramatic decline at low frequencies. Ac conductivity exhibited linear behavior with logarithmic frequency in the 105–106Hz region, indicating charge carrier hopping. There is no change in their behavior at any temperature at lower ranges (less than 100KHz). Declining temperature and frequency have been correlated with an increase in ac conductivity.

The effects of doping Zn on $\text{Cu}_{0.5}\text{Tl}_{0.5}\text{Ba}_2\text{Ca}_2\text{Cu}_{3-x}\text{Zn}_x\text{O}_{10-\delta}$ ($x=0,1.0,1.5,2.0,2.5$) samples were studied by N.A. Khan (**Khan et al., 2008**). They used a two-step solid state reaction approach to synthesis their samples as pellets. They used a four-probe resistivity measurement technique, the mutual induction method for sensitivity, and an LCR meter to measure the dielectric properties of their samples. They measured ac conductivities, tan losses, and real and imaginary components of the dielectric constants. They noticed that $T_c(R=0)$ and ac sensitivity rose consistently as Zn doping was increased. Consequently, the samples' diamagnetic properties are improved. The real part of the dielectric constant was shown to behave in a rising manner with increasing Zn concentration when the dielectric measurements were made at the frequencies of 10kHz and 10MHz. Tan losses were thereby reduced at 79K and the room temperature. They claimed that an increase in charge carrier concentration, which also increases polarization density, caused an increase in the real component of the dielectric constant. Additionally, they noticed a diminishing behavior with rising frequency for the imaginary portion of the dielectric constant. In other words, we can say that the imaginary portion of the dielectric constant decreased as the Zn concentration grew. In contrast to metallic copper with a partially full 3d9 shell, Zn had a lower conductivity because its 3d10 shell was filled, leading to a semiconductor with a tiny band gap. Due to better charge carriers, ac conductivity was boosted up to 2MHz, but once that frequency was reached, they found that conductivity returned to its normal state value.

At a concentration of $x=0-1.00\text{wt}\%$, M. Mumtaz connected Ni nanoparticles to a $\text{Cu}_{0.5}\text{Tl}_{0.5}\text{Ba}_2\text{Ca}_2\text{Cu}_3\text{O}_{10-\delta}$ superconducting matrix (**Mumtaz & Asghar, 2018**). Using a solid state reaction technique, $\text{Cu}_{0.5}\text{Tl}_{0.5}\text{Ba}_2\text{Ca}_2\text{Cu}_3\text{O}_{10-\delta}$ superconductors' phases were made, whereas the approach used to make nanoparticles was sol-gel. Using an LCR meter with a frequency range of 10 kHz and 10 MHz and a temperature range of 78K to 290K, the dielectric characteristics were studied. They estimated the real and imaginary components of the dielectric constant, tan losses, and ac conductivity in dielectric data. The energy stored in the sample is

shown in the real portion, whereas the energy lost during the application of external force is shown in the imaginary portion. Their graph demonstrated a consistent real component decline toward zero with increasing frequency, demonstrating that the polarisation time span is longer than the external ac signal. The real portion of the dielectric constant decreased by up to 0.72 weight percent, with greater values discovered at the greatest concentration of $x=1.00$ weight percent. An increase in the number of charge carriers trapped at grain boundaries was the cause of the value's rise. The imaginary component initially had higher values at lower frequencies before finally falling as the frequency rose. This behavior showed that the charge carriers were moving at lower ac signal frequencies. However, as the frequency was raised, the polarization's time span likewise rose, surpassing the ac signal. They have noticed a decrease in the flow of charge carriers as a result. The imaginary portion of the dielectric constant was initially reduced with the addition of Ni nanoparticles before beginning to increase at all temperatures. Higher imaginary part values indicate more energy losses, which were caused by high potential barriers created by Ni nanoparticles. They discovered a peak in the graph of tan loss, indicating that the resonance phenomena resulted from the superposition of the applied frequency and carrier frequency. At all temperatures, higher ac conductivity was observed in relation to the applied frequency, indicating enhanced hopping electron conditions.

The effects of Cd doping at the Cu site were examined in samples $\text{Cu}_{0.5}\text{Tl}_{0.5}\text{Ba}_2\text{Ca}_3\text{Cu}_{4-x}\text{Cd}_x\text{O}_{12-\delta}$ ($x=0,0.25,0.5,0.75$) by M. Rahim (**Rahim et al., 2013**). They used a two-step solid state reaction process to synthesis their samples, which they then palletized. They classified their samples using the XRD technique for the investigation of the crystal structure, the four-probe method for resistivity measurements, the mutual induction method for ac susceptibility, and an LCR meter for dielectric measurements. According to the structural study, the samples are tetragonal in shape, and the length of the c-axis increased as the concentration of Cd did. It resulted from the damped harmonic oscillations of Cd atoms in CuO_2 planes with masses larger than Cu. They observed a decrease in $T_c(R=0)$ with increasing Cd content. Due to the suppression in superconductivity, this restricts the population of electron-phonon interactions. The imaginary portion of the dielectric constant indicates the energy lost during the application of an external field, whereas the real portion represents the energy held in the samples. Due to negative capacitance, the actual component has negative values at all temperatures, and as frequencies are added, it gradually approaches zero. Due to the heavier Cd atoms' harmonic oscillations, which

reduced polarization density, the amplitude of the real component dropped. With an increase in temperature and frequency, the pattern of the imaginary component decreased. The decreased losses in Cd doped samples demonstrated the presence of Cd atoms across defect and grain boundaries. Lower cross sections of charge carriers were reflected by the decline in ac conductivity values with decreasing temperature. A decrease in the population of electron phonon interactions was demonstrated by samples that were Cd doped having higher conductivity levels.

I. Younes studied the dielectric characteristics of samples of $(\text{CH})_{nx}/(\text{Cu}_{0.5}\text{Tl}_{0.5})\text{Ba}_2\text{Ca}_3\text{Cu}_4\text{O}_{12-\delta}$ with different amounts of graphene ($0 \times 0.1\text{wt}\%$) (Younes et al., 2019). They used the conventional one-step solid-state reaction technique to produce their samples, which were in the shape of pallets. For the structural analysis of the sample, an X-ray diffractometer was used. Four-probe resistivity measurements, FTIR measurements between 400 and 700 cm^{-1} , a mutual induction method for ac susceptibility, and LCR meters for dielectric measurements involving real and imaginary parts, tan losses, and ac conductivity were also used. Based on XRD investigation, the lattice parameters revealed unsymmetrical heterogeneity at different graphene concentrations. They therefore assumed that adding graphene did not change the crystal structure but rather filled the spaces between the grains. It was found that the ideal concentration was $x=0.04\text{wt}\%$, and that excessive concentrations made it difficult to formulate the required phases. They saw an increase in the zero resistivity critical temperature, which denotes a rise in the conduction between grains that were connected by the accumulation of graphene at voids.

N. A. Khan studied the superconducting $\text{Cu}_{0.5}\text{Tl}_{0.5}\text{Ba}_2\text{Ca}_2\text{Cu}_{3-x}\text{M}_x\text{O}_{10-\delta}$ ($\text{M}=\text{Cd},\text{Zn},\text{Ni}; x=0,1,5$) compounds' dielectric reaction (Khan et al., 2018). They used the solid state reaction approach to manufacture their samples, which were created in the shape of pallets. They used the XRD technique for structural analysis, a four-probe approach for resistivity measurements, a joint inductance method for ac susceptibility, FTIR measurements between 400 and 700 cm^{-1} , and an LCR metre for dielectric measurements. The orthorhombic structure of all the doped samples was shown by the XRD data, and the c-axis length increased with the doping concentration. $T_c(R=0)$ decreased with Cd doping while rising with Ni and Zn doping. All doped samples have a decrease in ac resistance, but Cd doped samples experience the most drop. In all doped samples, the real component of the dielectric constant's negative values and imaginary part's

positive values were suppressed with increasing frequency at all temperatures. The maximum suppression seen in the Cd doped sample is due to a hormonal oscillation in the CuO/CdO plane. Tan losses show resonance peaks in both doped and un-doped samples because the applied frequency and the polarizations frequency of the interfaces match. They found that ac conductivity decreased as frequency and temperature rose.

Chapter # 3

3 Experimental Methods

In this chapter, we will briefly go into the synthesis of thallium-based titanium-doped CuTI 1212 superconductors. We will also go through the methods used to characterize these materials. These methods include DC resistivity measurement, XRD (X-ray diffraction), FTIR (Fourier transform infrared spectroscopy), FIC (fluctuation induced conductivity analysis), and dielectric measurement.

3.1 Sample preparation:

$\text{Cu}_{0.5}\text{Tl}_{0.5}\text{Ba}_2\text{CaCu}_{2-x}\text{Ti}_x\text{O}_{8-\delta}$ were synthesized using the two-step solid state reaction technique, with $x=0, 0.5, 1, 1.5,$ and 2 . Here, the substances $\text{Ba}(\text{NO}_3)_2$, CaCO_3 , Tl_2O_3 , and TiO were chosen. We used TiO for the doping of titanium. The necessary compounds were mashed in a mortar and pestle for an hour. The grounded material was then loaded onto a quartz boat and heated to 840°C for 24 hours in a preheated furnace.

The sample was cooled to room temperature after 24 hours. The material was then crushed for an additional hour before being re-inserted into the furnace for a further 24 hours in alumina boats. The thallium is added to the precursor $\text{Cu}_{0.5}\text{Tl}_{0.5}\text{Ba}_2\text{CaCu}_{1.5}\text{Ti}_{0.5}\text{O}_{8-\delta}$ after it has already been made, and the mixture is again processed for an additional hour. Following that, the material is palletized using 3.8 tons/cm^2 of pressure. The pallets are then wrapped in gold foil and sintered in a furnace for ten minutes. At room temperature, it is subsequently cooled. During sintering, the gold capsule stops thallium from being lost.

3.2 Characterization Methods:

The following are the methods utilized to characterize our superconducting samples.

- X-Ray Diffraction (XRD)
- Electrical resistivity measurements (RT)
- Fourier transform infrared spectroscopy (FTIR)
- Dielectric measurements and ac conductivity
- Fluctuation induced conductivity analysis (FIC)

3.2.1 X-Ray Diffraction (XRD):

The information provided by XRD is used to determine the thickness of films as well as the crystal structure of the material, lattice parameters, grain size, defect structure, and epitaxy porosity (Robertson, 1986). The main information it provides about the sample is whether or not it is crystalline. Before XRD, it was believed that solid materials have periodic arrangements of atoms, but there was no experimental proof for this. The development of XRD has improved scientists' ability to comprehend the crystal structure of many materials.

X-rays are utilised to determine the crystal structure since their wavelength is similar to the distance between individual atoms. It serves as a grating in nature. An extremely high energy beam is an X-ray. with a wavelength that is equivalent to the interplanar spacing, 0.5 to 2.5. Cu and Mo sources are the most frequent producers of energetic X-rays.

3.2.1.1 X-ray photon's energy:

The X-ray photon's energy is:

$$E = h\nu \quad (3.1)$$

OR,

$$E = hc/\lambda$$

Where,

$$\lambda = 0.0998\text{nm, as } hc = 1240 \text{ ev.nm}$$

Thus,

$$E = 12.42 \text{ Kev}$$

Since all crystals are constructed of parallel planes, the distance spanned by two parallel X-ray beams must be an intrinsic multiple of the wavelength employed for X-ray diffraction. Bragg's Rule is the name given to this circumstance.

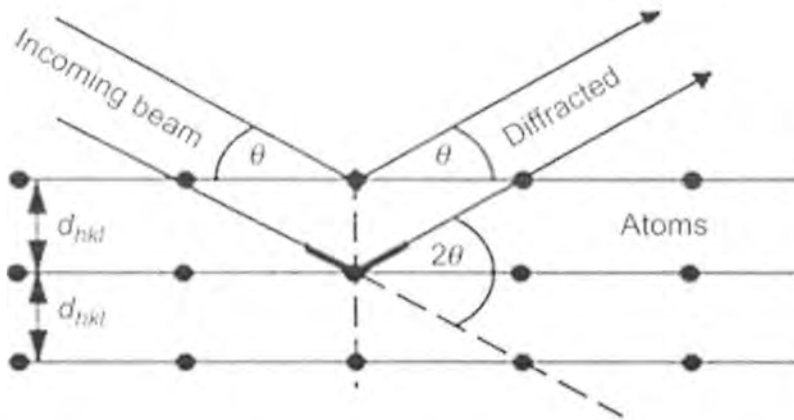


Figure 3.1 Schematic diagram of X-ray diffraction through crystal

The path difference between two parallel x-rays is given by:

$$xy + yz = \text{Path difference}$$

According to Bragg's law, the wavelength used for constructive interference must have an integral multiple of the path difference.

$$xy + yz = n\lambda$$

$$xy = yz = d \sin \theta$$

So, we get.

$$2d \sin \theta = n\lambda \quad (3.2)$$

Where "d" is the interplanar separation, "theta" denotes the diffraction angle, "n" denotes a positive integer, and "lambda" denotes the X-ray wavelength.

XRD analysis is being used to characterize the earlier generated samples. We used the Bruker D8 Focus XRD machine. It utilizes the powder diffraction technique. Cu is employed as an X-ray source with 1.5406 wavelength k lines. The utilized range for "2theta" is 460o. 0.8 seconds each step was the fixed scan speed. On a computer system, the diffraction data is gathered.

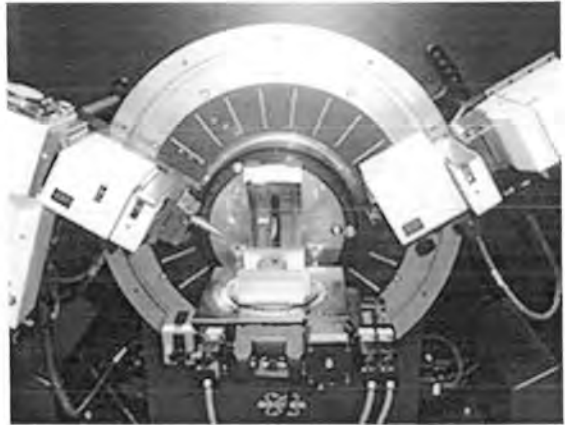
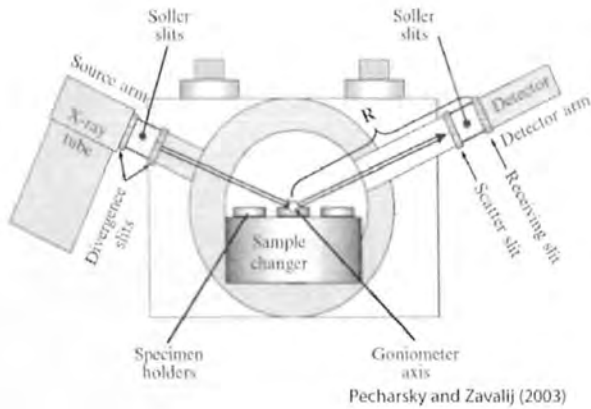


Figure 3.2 Working of XRD

Using check-cell software, the structural data is recovered from the data. It provides details regarding the lattice parameters a, b, and c. The volume of the unit cell is computed using the values of a, b, and c. Finally, the graphs are created using origin software, and the hkl values are noted on the corresponding peaks.

Using the Debye-Scherrer equation, the samples' crystallite sizes are determined.

$$D = \frac{k\lambda}{B\cos\theta} \quad (3.3)$$

Where "k" is equal to 0.9, " λ " is equal to 1.5406 degrees, " θ " is the angle of diffraction, and " β " is full width at half maxima.

3.2.1.2 ADVANTAGES AND DISADVANTAGES OF XRD:

Following are some XRD advantages and disadvantages.

- X-ray diffraction is a popular technique.
- X-ray diffraction is a practical and affordable method.
- The sample does not need to be placed in a vacuum because air does not readily absorb X-rays.
- X-ray diffraction is a quick, simple, and less harmful method.

- Photographic film is capable of detecting X-rays.
- Lighter atoms can't interact with X-rays very strongly.
- It is impossible for X-rays to differentiate between various isotopes of the same element.

3.2.2 ELECTRICAL RESISTIVITY MEASUREMENT (RT):

The main causes of electrical resistivity are temperature (T) and average time (τ).

3.2.2.1 Average Time Dependence:

When an external electrical field is supplied to the sample, the atoms' electrons accelerate and start colliding with one another. As a result, information about the atoms' resistance to electron motion is given. The resistance is caused by resistance and collision, and it is provided by:

$$\rho = \frac{m}{n\tau e^2} \quad (3.4)$$

Where $1/\tau$ is the probability of an electron collision (scattering) per unit time, 'n' is the number density, " ρ " is the resistivity, " τ " is the average duration between two collisions, and "m" is the mass of the electron. Every crystal contains flaws, as we all know. Therefore, as electrons are flowing, they may collide with lattice phonons. As a result, the likelihood of an electron colliding (scattering) is equal to the sum of the probabilities caused by phonon scattering ($1/\tau_{ph}$) and lattice defects ($1/\tau_i$). Hence total probability is:

$$\frac{1}{\tau} = \frac{1}{\tau_{ph}} + \frac{1}{\tau_i} \quad (3.5)$$

Thus, resistivity is:

$$\rho = \rho_{ph} + \rho_i \quad (3.6)$$

The ideal resistivity, " ρ_{ph} ", is temperature-dependent, whereas the residual resistivity, " ρ_i ", is not temperature-dependent (MN Rudden, 1971).

3.2.2.2 Temperature Dependence:

When temperature of a superconducting sample increases, the collision of electrons with the atoms also increases so resistance increases and when sample is cooled (temperature is lowered) then collision with atoms decreases so resistance decreases. And we know that the temperature dependent resistivity " ρ_{ph} " is due to phonons. So at low temperature, the dependence of resistivity on temperature is of the order of T^5 and it is confirmed for alkali metals. In simple metals, at high temperatures, the dependence of resistivity on temperature is the mean square amplitude of phonons.

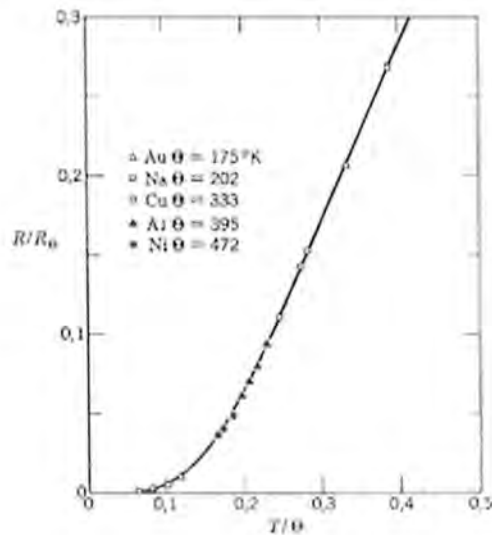


Figure 3.3 The phonon contribution to the resistivity in normal metals.

3.2.2.3 Electrical resistivity measurements:

We may determine a superconducting sample's critical temperature or " T_c " using DC electrical resistivity. This measurement aids in our analysis of the sample's properties in both the superconducting and normal states. Utilizing the four probe approach, which is based on Ohm's Law, DC-electrical resistivity, is determined.

$$V = IR$$

Where " I " stands for applied current, " V " for voltage and " R " for conductor resistance.

Experimentally, the resistance is inversely related to cross-sectional area (" A ") and directly related to conductor length (" L "). So:

$$R \propto L$$

Also,

$$R \propto \frac{1}{A}$$

So we can say

$$R \propto \frac{L}{A}$$

It means,

$$R \propto \rho \frac{L}{A}$$

Where " ρ " denotes the resistivity, a function of temperature:

$$R(T) \propto \rho(T) \frac{L}{A}$$

$$\rho(T) \propto R(T) \frac{A}{L} \quad (3.7)$$

However, from Ohm's law

$$R(T) = \frac{V}{I}$$

$$\rho(T) = \frac{VA}{IL}$$

$$\rho(T) = \frac{VA}{IL} \quad (3.8)$$

The resistivity is measured in units of $\Omega\cdot\text{m}$ if the following values are used: area ' A ' in m^2 , length ' L ' in m, current ' A ' in amperes, and voltage ' V ' in volts.

3.2.2.4 Resistivity Measurement Methods:

Resistance and the structure (shape) of a sample, such as whether it is in the form of powder, a single crystal film, or small crystalline, are two factors that influence the suitability of procedures. (Marton, L.; Lark-Horovitz, K.; Johnson, 1959)

Our superconducting samples are made of copper-thallium-based pellets (small crystals). Equation (3.8), where "I" denotes the constant current and "V" denotes the voltage drop across the superconducting sample, can be used to determine the resistivity.

3.2.2.5 Four Probe Method for resistivity:

This setup is widely used for the resistivity measurements. The experimental setup for the four-probe approach is shown in Fig. 3.4.

Four contacts are attached to the surface of the superconducting sample using this method, and the connections are made using silver paste. While the two inner contacts move the voltage drop across the superconducting sample, the two outside contacts carry the current "I" through it. This method can be used to determine the voltage drop between probes 1 and 2, the current "I" flowing through probes 3 and 4, the distance "D" between probes 1 and 2, and the cross-sectional area "A". A current of around 1 mA is utilized in this resistivity test, and the voltage is recorded for each temperature range between ambient temperature and liquid nitrogen where the sample is kept. Making a thermocouple that measures temperature in mV allows one to calculate the sample's temperature. Liquid nitrogen is used to chill the sample since superconductivity only occurs below room temperature. A list of resistance values corresponding to a temperature value is produced by this method. The resistivity can be measured if the resistance value is known. This method enables us to plot a graph between resistance and temperature that indicates whether or not a superconductor is forming. If the graphed transition occurs suddenly, we have successfully manufactured the superconductor.

Resistivity is correlated with,

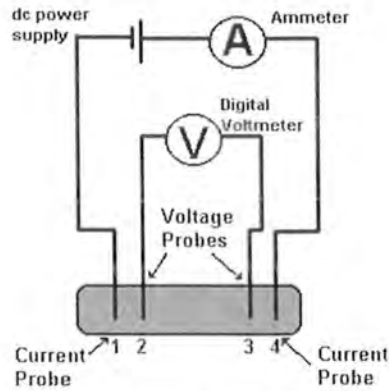


Figure 2: Schematic of Four-Point Probe

Figure 3.4 Schematic of four-point probe

3.2.3 Fourier Transform Infrared Spectroscopy:

Materials' atoms oscillate at a certain frequency around their average positions in solids. These oscillations are influenced by the atomic mass, the bond angle, and the bond length. Even at 0 K temperatures, their atoms are in motion. Lattice vibrations must be used to describe the physical characteristics of materials. A straightforward harmonic oscillation quantum mechanical approximation can be used to determine the energy associated with these lattice vibrations as follows:

for $n = 0, 1, 2, 3$

$$E_n = \left(n + \frac{1}{2} \right) \hbar \omega_0 \quad (3.9)$$

Here, the Boltzmann constant \hbar has a value of $\hbar = h/2\pi \sim 1.054 \times 10^{-34} \text{ J}\cdot\text{s}$ and " ω_0 " is the harmonic oscillator's frequency. These vibrations also have energy $E_0 = 1/2 \hbar \omega_0$ for ground state energy $n = 0$.

A substance's vibrational modes must first be identified in order to categorize it. To see these modes, we employ a method known as Fourier Transform Infrared Spectroscopy. (Markovich, Robert J, n.d.)

The components of FTIR are:

- ❖ Michelson Interferometer
- ❖ Light source or Laser
- ❖ Sample
- ❖ Detector
- ❖ Computer

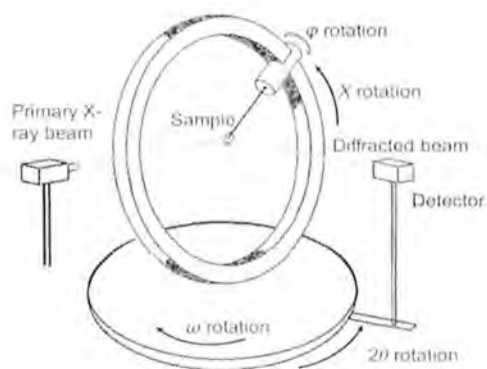


Figure 3.5: FTIR working

An essential component of FTIR is the Michelson interferometer, which comprises of a Moving mirror, a Fix mirror, a Detector, and a Beam splitter. Mirrors that are stationary or in motion are both planar and parallel. In these mirrors, one mirror is fixed while the other can move in an opposite direction. Another component of the FTIR apparatus is the beam splitter, which separates the source beam into two halves, one of which is reflected and the other of which is transmitted. The mirrored beam strikes, moves in the direction of the fixed mirror, and then reflects.

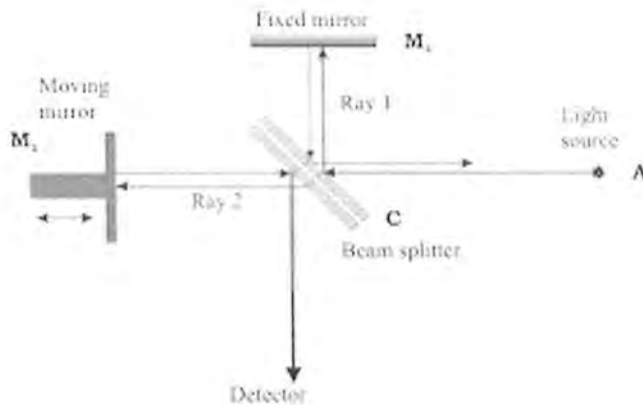


Figure 3.6 Schematic diagram of Michelson interferometer

An interferogram is the name given to the resulting ray produced when two reflected radiation beams interfere. An interferogram is created using the frequency data to show how much frequency the material has captured (sample) (Faix, 1992). The interferogram will convert the intensity vs. frequency IR band using Fourier transformation (“**Handbook of Instrumental Techniques for Analytical Chemistry,**” 1998). A bright source emits an infrared beam. This beam ultimately enters the detector after passing through the gap and controlling the energy that is injected into the sample.

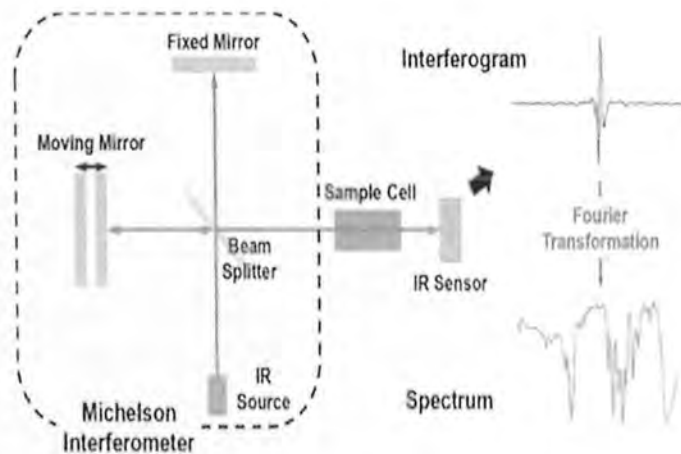


Figure 3.7 Schematic diagram of FTIR apparatus.

We used a Nicolet 5700 type spectrometer for our investigation. To investigate the vibrational modes in superconducting samples, the FTIR spectrum has the following measurements.

- ❖ A pure KBr pellet was first positioned in the beam's path as a backdrop, and 200 scans were performed with a range of 400–700 cm^{-1} .
- ❖ We combined 50 mg of KBr compound with 5 mg of superconductor, and then created a pellet under a pressure of 3.8 tons/ cm^2 . We performed 200 scans of the mixed sample spectrum with a 400-700 cm^{-1} range.
- ❖ The application only displayed the spectrum of our sample after removing the background spectrum because we utilized KBr as a source.
- ❖ OMNIC software tools were used to analyze and research the spectrum of our samples.

The following uses for FTIR are possible.

- ❖ Materials identification of unknown samples
- ❖ determining the quality of a material
- ❖ Estimating the amount of each component in a material

3.2.4 Dielectric measurements and ac conductivity:

We directly measured the conductance (G) and capacitance (C) in a certain frequency and temperature range (20Hz-1MHz and 80K-290K, respectively) using an LCR meter in order to determine the real and imaginary portions of the dielectric constants ϵ' and ϵ'' , dielectric loss ($\tan \delta$), and ac conductivity .

3.2.4.1 Method:

Calibrations were performed using a typical inductor and capacitor before measuring the readings from the LCR meter in order to identify any external circuit effects.

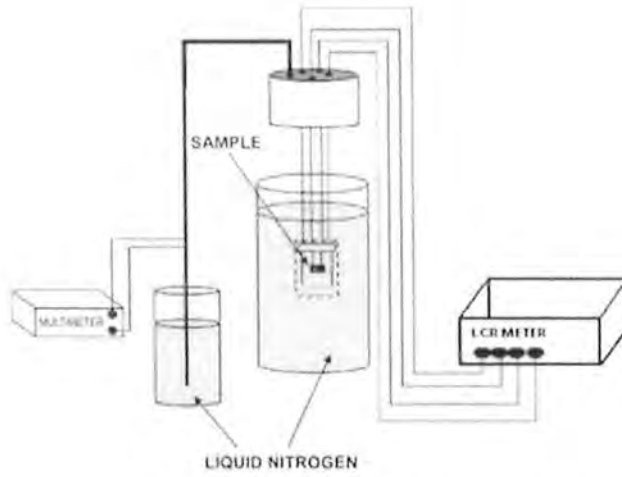


Figure 3.8 Experimental setup for dielectric properties

These calculations were performed in parallel. The calculations of the sample pellets were performed using a two probe approach. Thin conducting wires were attached to the silver electrode surfaces of the sample after the silver paste had been applied to both sides and cured at room temperature. The sample pellet was linked to an electrical connection, including an LCR metre, to determine capacitance and conductance as a function of frequency. The temperature of the samples used to make superconductors was lowered using liquid nitrogen. Following Equation was used to estimate the dielectric constant (ϵ_r' , ϵ_r''), I dielectric loss ($\tan\delta$), and ac conductivity (σ_{ac}) by computing capacitance (C) and conductance (G) at various frequencies and temperatures (Çavdar et al., 2005).

$$\epsilon_r' = Cd/A\epsilon_0$$

$$\epsilon_r'' = Cd/A\epsilon_0\omega$$

$$\tan\delta = \frac{\epsilon_r''}{\epsilon_r'}$$

$$\sigma_{ac} = 2\pi f\epsilon_0\epsilon_r'\tan\delta$$

where "A" denotes the electrode's surface area, "d" the thickness, "C" the capacitance, "G" the conductance, " $\omega(2\pi f)$ " the angular frequency, "F" the applied field's frequency, and ϵ_0 the permittivity of empty space.

3.2.5 Fluctuation induced conductivity analysis (FIC)

A technique for analyzing superconducting fluctuations created by the production and annihilation of Cooper pairs down to the onset temperature is known as "fluctuation induced conductivity analysis" or "para conductivity analysis." Cooper pairs begin to form above the transition temperature, but thermal turbulence causes them to keep forming and annihilating until $T_c(R=0)$. Superconductor fluctuates as a result of production and annihilation. The density of fluctuation reduced when we cooled our sample below $T_c(R=0)$, proving that thermodynamic fluctuation was ineffective in stopping the formation of a cooper pair. Condensation of the cooper pairs caused zero resistance as a result (**Rafique et al., 2014**). These fluctuations in induced conductivity are observed for a temperature regime about T_c , referred to as the Ginzburg criterion temperature (T_G). For low temperature superconductors, T_G is less than 1 K, whereas for high temperature superconductors, it is between 1-2 K. Therefore, these variations could be looked at. As shown by the relationship below, Ginzburg was the first scientist to investigate how heat capacity fluctuations function and to develop the temperature value at which fluctuation adjustment to heat capacity is crucial.

$$\frac{\Delta T}{T_c} \sim \left[\frac{(T_c)^4}{\epsilon_f} \right] \sim \left[\frac{(\alpha)^4}{\xi} \right] \sim 10^{-4} \text{ to } 10^{-16}$$

Here, "a" stands for the interatomic distance between two lattice sites, and " ξ " stands for the coherence length. Since $\Delta T/T_c$ has such a small value, these changes have long been experimentally undetected.

Due to the variation that caused conductivity to deviate noticeably from its linear dependency at higher temperatures, given as

$$\Delta\sigma(T) = \frac{\rho_n(T) - \rho(T)}{\rho_n(T)\rho(T)}$$

Here, the real resistivity is denoted by $\rho(T)$, and the projected resistivity for the normal state is given by $\rho_n(T) = \alpha + \beta T$. Two distinct types of fluctuation are typically regarded as $\Delta\sigma(T)$. The first one is the Aslamazov-Larkin (AL) contribution, which is a result of excess current caused by Cooper pair variations at temperatures higher than T_c (Aslamazov & Larkin, 1968). The second one, by Maki-Thompson (MT), reported the impact of superconducting carrier oscillations on the conductivity of ordinary electrons. The crossover point between a three-dimensional (3D) electronic state and a two-dimensional (2D) electronic state is shown by a different model called the Lawrence-Doniach (LD) model. The MT term has a large impact in the 2D fluctuation area for mild pair breaking, whereas the AL term has a dependence on phase-relaxation time τ_ϕ and is found close to T_c (Muzaffar & Khan, 2016). The superconductor's dimensionality, phase relaxation time τ_ϕ , and coherence length $\xi_c(T)$ are all usefully revealed by FIC. Numerous scholars have supported the examination of crossover temperatures using the LD model, however due to the MT contribution's limited ability to evaluate, few academics were persuaded.

Although the results are slightly different from thin films, FIC analysis of polycrystalline bulk material is generally compatible with the feature of 3D fluctuation. 3D to 2D crossover has been observed in thin films with significant c-axis orientation. Temperature range affects how well 3D fluctuations or 2D-3D crossover perform. Different experimental outcomes for a single crystal have been discovered (Hagen et al., 1988).

Chapter # 4

4 Results & Discussion

4.1 Introduction:

Two conducting CuO_2 samples and a $\text{Cu}_{0.5}\text{Tl}_{0.5}\text{Ba}_2\text{O}_{4-\delta}$ charge reservoir are included in the $\text{Cu}_{0.5}\text{Tl}_{0.5}\text{Ba}_2\text{CaCu}_2\text{O}_{8-\delta}$ superconductor. Due to its higher Fermi level, the charge reservoir layer provides carriers to the conducting CuO_2 planes, and the superconductivity results from interactions between the carriers and lattice atoms in the planes (Xiao et al., 1988). In the conducting CuO_2 planes, there may be two different forms of phonons in the atoms' lattice vibrations. In their $3d^9$ form, copper atoms have a tiny spin, and when these atoms vibrate at a certain temperature, the consequence is oscillating spin density waves. A compound's ability to conduct electricity at a specific critical temperature is controlled by lattice vibrations (phonons), and since the moving atoms have a tiny spin, this causes oscillating spin densities that interact with charge density waves to produce superconductivity. The question of whether electron-phonon interactions play any part in the mechanism underlying high T_c superconductivity arises? When heavier than Cu atoms are doped at the CuO_2 planar sites, softer phonons and asymmetric oscillations are produced, whereas when lighter than Cu atoms are doped there, harsher phonons and related asymmetries are produced (Bandyopadhyay et al., 1994). The spin configurations and thus the spin densities of the doped atoms may be influenced by their charge state. There is a tolerable limit for spin scattering of doped atoms at the CuO_2 planar sites depending on their charge state, but depending on the mass of doped atoms, harsher or softer phonons are produced in the solid state medium.

In a solid-state medium, lighter atom oscillations yield harder phonons, whereas heavier atom oscillations result in soft phonons. By doping Ti at the CuO_2 planar sites in such superconductors by creating $\text{Cu}_{0.5}\text{Tl}_{0.5}\text{Ba}_2\text{CaCu}_{2-x}\text{Ti}_x\text{O}_{8-\delta}$ ($x=0, 0.5, 1, 1.5, 2$) sample, the involvement of such phonons in the mechanism of high T_c superconductivity in $\text{Cu}_{0.5}\text{Tl}_{0.5}\text{Ba}_2\text{CaCu}_2\text{O}_{8-\delta}$ superconductors is studied.

4.2 Experimental:

$\text{Ca}(\text{NO}_3)_2 \cdot 4\text{H}_2\text{O}$, $\text{Ba}(\text{NO}_3)_2$, CaCO_3 , $\text{Cu}_2(\text{CN})_2 + \text{H}_2\text{O}$, Ti_2O_3 are used as starting compounds in a two-step solid state reaction process to create $\text{Cu}_{0.5}\text{Tl}_{0.5}\text{Ba}_2\text{CaCu}_{2-x}\text{Ti}_x\text{O}_{8-\delta}$ ($x=0, 0.5, 1, 1.5, 2.0$) samples.

$\text{Cu}_{0.5}\text{Tl}_{0.5}\text{Ba}_2\text{CaCu}_{2-x}\text{Ti}_x\text{O}_{8-\delta}$ ($x=0, 0.5, 1, 1.5, 2.0$) samples were prepared by mixing these compounds in the proper ratios for roughly an hour in an agate mortar and pestle. The mixture was then twice fired at 840°C in a preheated chamber for 24 hours, followed by furnace cooling to room temperature. The material is fired in two stages, the first in a quartz boat and the second in an alumina boat. The initial firing in the quartz boat is necessary to prevent the reactivity of the disintegrating constituents with the boat material. In contrast, the second fire does not require a quartz boat because the constituent reaction has already taken place. To obtain $\text{Cu}_{0.5}\text{Tl}_{0.5}\text{Ba}_2\text{CaCu}_{2-x}\text{Ti}_x\text{O}_{8-\delta}$ ($x=0, 0.5, 1, 1.5, 2.0$) samples as the final composition of the samples, the precursor material is combined with a calculated amount of Ti_2O_3 and ground again for around an hour. The resulting material is then compressed at 3.8 tons/cm^2 and powdered before being pelletized. The resultant pellets are sealed in a gold capsule, heated for 10 minutes at 840°C , and then quenched to room temperature. X-ray diffraction (XRD), temperature-dependent resistance measurements [$\rho(T)$], Fourier Transform Infrared (FTIR) absorption measurements, and excess conductivity analysis of conductivity data are used to characterise the generated samples. The cell parameters were calculated by a cell refinement computer programme utilising Check Cell software, and the structure phases of these materials were identified by an X-ray diffraction scan, Bruker DX 8 Focus using a $\text{CuK}\alpha$ source of wavelength 1.54056 . The temperature-dependent resistance of these samples was measured using the traditional four-probe method. The Fourier Transform Infrared spectrometer NICOLET 5700 was used to detect the FTIR absorption. Using KBr as a background material, the FTIR absorption measurements were carried out in the wavenumber range of $400\text{-}700\text{cm}^{-1}$.

Using the two-probe technique, frequency dependent dielectric measurements of $\text{Cu}_{0.5}\text{Tl}_{0.5}\text{Ba}_2\text{CaCu}_{2-x}\text{Ti}_x\text{O}_{8-\delta}$ ($x=0, 0.5, 1, 1.5, 2.0$) samples are performed on a Wayne Kerr 4275 LCR Meter with a frequency range of $20\text{-}3000\text{Hz}$. Silver paste was used to make contacts on the sample's surface, and measurements were performed at 80K . The following formulas were

used to calculate the dielectric constant (ϵ_r), dielectric loss ($\tan\delta$), and ac-conductivity (σ_{ac}) of the samples by measuring their conductance (G) and capacitance (C) (Çavdar et al., 2005).

$$\epsilon_r = \epsilon_m / \epsilon_0 \quad (3.1)$$

Where,

ϵ_m = permittivity of material

ϵ_0 = permittivity of free space

ϵ_r = relative permittivity

$$\epsilon' = Cd/A\epsilon_0 \quad (4.2)$$

Where

C = capacitance of the pellet (F),

d = thickness of the pellet (m),

ϵ_0 = permittivity of free space ($\epsilon_0 = 8.85 \times 10^{-12}$ F m⁻¹)

A = area of the electrode (m²).

The measured conductance values (G) from the relation were used to compute the imaginary component of the dielectric loss (ϵ'') of the various frequencies.

$$\epsilon'' = Gd/A\epsilon_0\omega \quad (4.3)$$

Where

G = dc conductance of the sample

$\omega = (2\pi f)$ = angular frequency.

From the below relation, the dielectric loss $\tan \delta$ is computed

$$\tan\delta = \varepsilon''/\varepsilon' \quad (4.4)$$

Using the below relation, the conductivity σ_{ac} of alternating current (ac) is determined

$$\sigma_{ac} = 2\pi f \varepsilon_0 \varepsilon' \tan\delta \quad (4.5)$$

Where f is the applied ac field's frequency (Hz).

4.3 Result and Discussions:

4.3.1 X-ray Diffraction:

Figure 4.1 shows the results of an X-ray diffraction scan of samples of $\text{Cu}_{0.5}\text{Tl}_{0.5}\text{Ba}_2\text{CaCu}_{2-x}\text{Ti}_x\text{O}_{8-\delta}$ ($x=0, 0.5, 1, 1.5, 2.0$). The figure indexes the diffraction lines in the spectra that were fitted to the orthorhombic crystal structure using the PMMM space group. The cell parameters are calculated using the Check-cell computer program, and they are shown in Fig. 4.2: (a,b).

Ti doping causes the a- and b-axes to be suppressed while lengthening the c-axis. With the rise in Ti doping in the final product, the volume of the unit cell is suppressed (except from the $x=0.5$ Ti-doping), as shown in Fig. 4.3. The antiferromagnetic order at the CuO_2 planar site is most likely broken in the samples with Ti-doping of $x=0.5$, which somehow causes an increase in the volume of the unit cell.

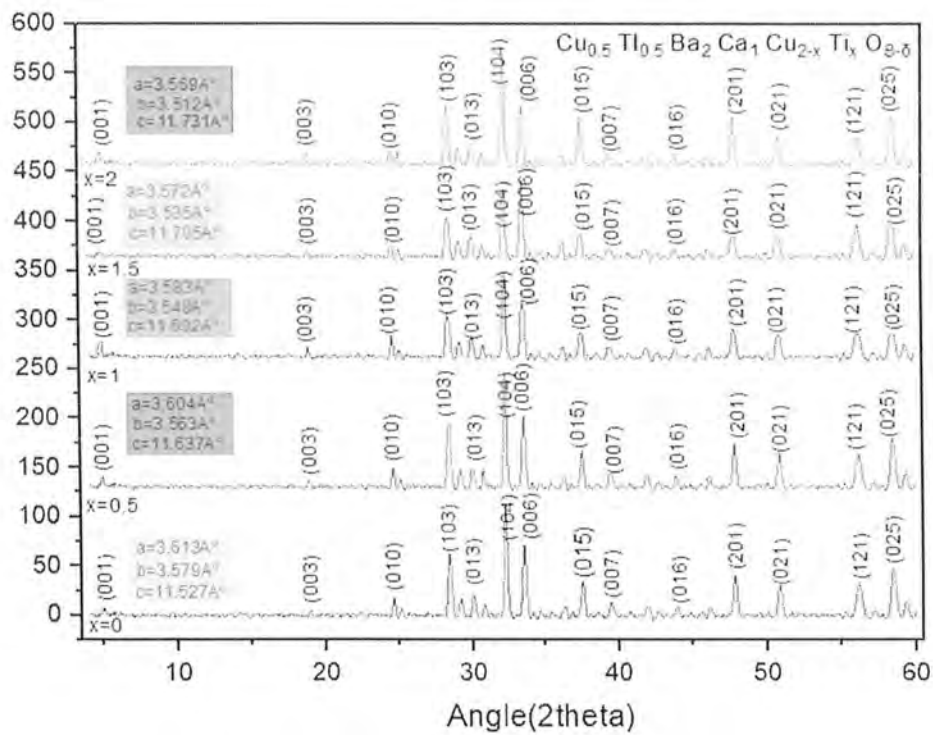


Figure 4.1 Shows the X-ray diffraction spectra of $\text{Cu}_{0.5}\text{Ti}_{0.5}\text{Ba}_2\text{Ca}_1\text{Cu}_{2-x}\text{Ti}_x\text{O}_{8-\delta}$ ($x=0, 0.5, 1, 1.5, 2.0$) samples.

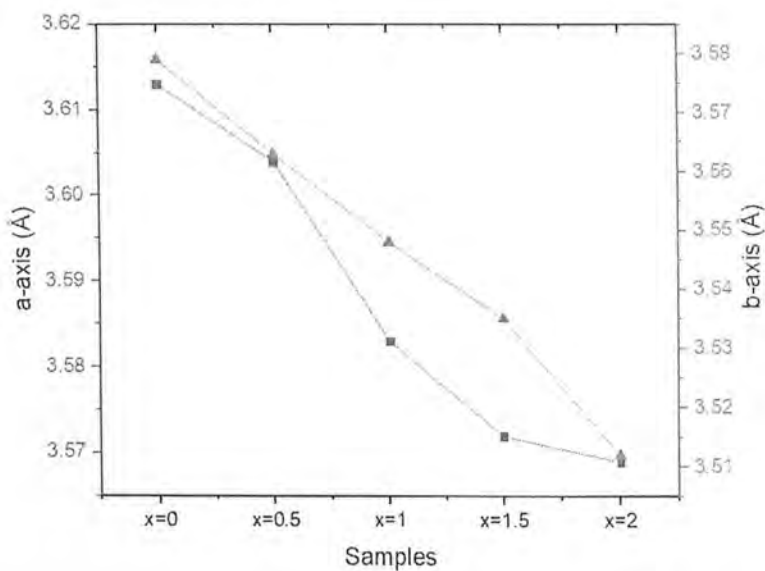


Figure 4.2 The a and b-axis comparison of $\text{Cu}_{0.5}\text{Ti}_{0.5}\text{Ba}_2\text{Ca}_1\text{Cu}_{2-x}\text{Ti}_x\text{O}_{8-\delta}$ ($x=0, 0.5, 1, 1.5, 2.0$) samples with Ti-doping

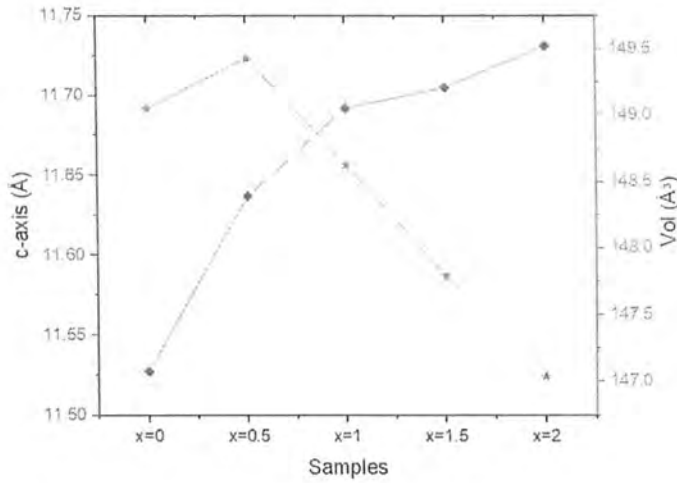


Figure 4.3 The c-axis and volume comparison of $\text{Cu}_{0.5}\text{Ti}_{0.5}\text{Ba}_2\text{CaCu}_{2-x}\text{Ti}_x\text{O}_{8-\delta}$ ($x=0, 0.5, 1, 1.5, 2.0$) samples with Ti-doping

4.3.2 Resistivity Measurements:

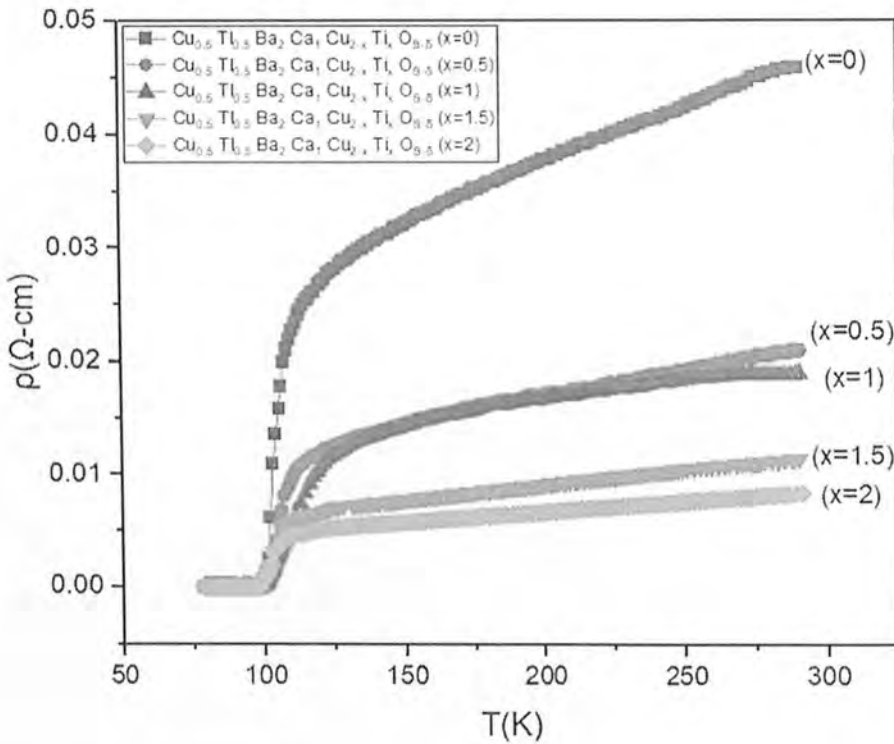


Figure 4.4 Resistivity versus temperature measurements of $\text{Cu}_{0.5}\text{Ti}_{0.5}\text{Ba}_2\text{CaCu}_{2-x}\text{Ti}_x\text{O}_{8-\delta}$ ($x=0, 0.5, 1, 1.5, 2.0$) samples

Sr No	Sample	$T_c(R=0)$	$T_c(\text{onset})$
1	x=0	98.95 (K)	111.32 (K)
2	x=0.5	100.25 (K)	110.63 (K)
3	x=1	100.06 (K)	111.95 (K)
4	x=1.5	99.83 (K)	111.57 (K)
5	x=2.0	100 (K)	109.52 (K)

Table 2 $T_c(R=0)$ and $T_c(\text{onset})$ temperatures of $\text{Cu}_{0.5}\text{Tl}_{0.5}\text{Ba}_2\text{CaCu}_{2-x}\text{Ti}_x\text{O}_{8-\delta}$ (x=0, 0.5, 1, 1.5, 2.0) samples

Fig 4.4 displays the resistivity measurements of $\text{Cu}_{0.5}\text{Tl}_{0.5}\text{Ba}_2\text{CaCu}_{2-x}\text{Ti}_x\text{O}_{8-\delta}$ (x=0, 0.5, 1, 1.5, 2.0) samples as a function of temperature (a, b, c, d, e). The increased Ti-doping demonstrates greater carrier density at the CuO_2 planar sites, which results in an elevated metallic character in the final compound and consistently decreases the resistivity of samples at room temperature. All of these samples exhibit metallic resistance fluctuations from room temperature down to onset of superconductivity. $\text{Cu}_{0.5}\text{Tl}_{0.5}\text{Ba}_2\text{CaCu}_{2-x}\text{Ti}_x\text{O}_{8-\delta}$ (x=0, 0.5, 1, 1.5, 2.0) samples exhibit superconductivity at temperatures of 111.3, 110.6, 112, and 109.5 K, respectively, and the zero resistivity critical is at 99, 100.3, 100, 99.8, and 100 K. The fact that a compound with all of the CuO_2 planes removed and all of the TiO_2 planes present exhibits superconductivity at 100K is surprising.

Superconductivity over 77K has been seen in $\text{Cu}_{0.5}\text{Tl}_{0.5}\text{Ba}_2\text{CaTi}_2\text{O}_{8-\delta}$ samples, and this has crucial ramifications for understanding the process of high T_c superconductivity in such compounds. Small spin is possessed by copper atoms in the $\text{Cu } 3d^9$ state, and because they are completely absent from $\text{Cu}_{0.5}\text{Tl}_{0.5}\text{Ba}_2\text{CaTi}_2\text{O}_{8-\delta}$ samples, there is no evidence that small spin is involved in the final compound's mechanism for high T_c superconductivity. Alternatively, higher order spin-carrying Ti atoms in the $3d^2$ state may also play a similar role in this mechanism.

To prove this, samples of $\text{Tl}_{0.5}\text{Ti}_{0.5}\text{Ba}_2\text{CaTi}_2\text{O}_{8-\delta}$ without Cu atoms in the final molecule were produced under the same conditions. $\text{Cu}_{0.5}\text{Tl}_{0.5}\text{Ba}_2\text{CaTi}_2\text{O}_{8-\delta}$ samples' resistivity data are depicted in Fig. 4.5 variable range hopping (VRH) conductivity and Fig. 4.6 relationship of the form:

$$\rho(T) = \rho_0 \exp \left[\left(\frac{T_0}{T} \right)^{1/4} \right] \quad (4.6)$$

The Mott 3D VRH type conduction mechanism (with $b = 1/4$) was used to analyze the ρ - T data of the various samples [...].

The experimental data from our samples continue to fit well with the Mott 3D VRH model. According to Fig. 4.6, the inset shows the plot of $\ln \rho$ vs. $1/T^{1/4}$ and the theoretical prediction for the Mott Varying Range Hopping (VRH) in 3D mechanism is indicated by a straight line with an activation energy of 2.09 Mev. $\text{Cu}_{0.5}\text{Tl}_{0.5}\text{Ba}_2\text{Ca}_2\text{Na}_3\text{O}_{10-\delta}$ has semiconductor-like resistivity variations with temperature fitted in the regime of 77K to 300K.

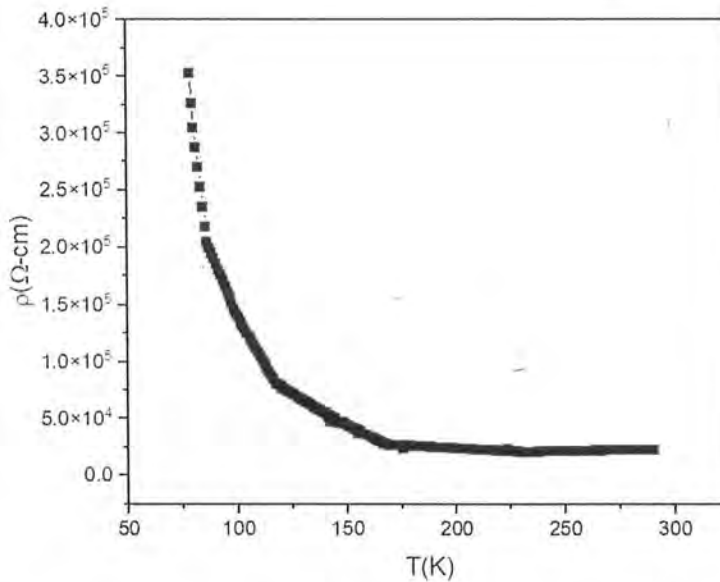


Figure 4.5 Resistivity versus temperature measurements of $\text{Tl}_{0.5}\text{Ti}_{0.5}\text{Ba}_2\text{CaTi}_2\text{O}_{8-\delta}$

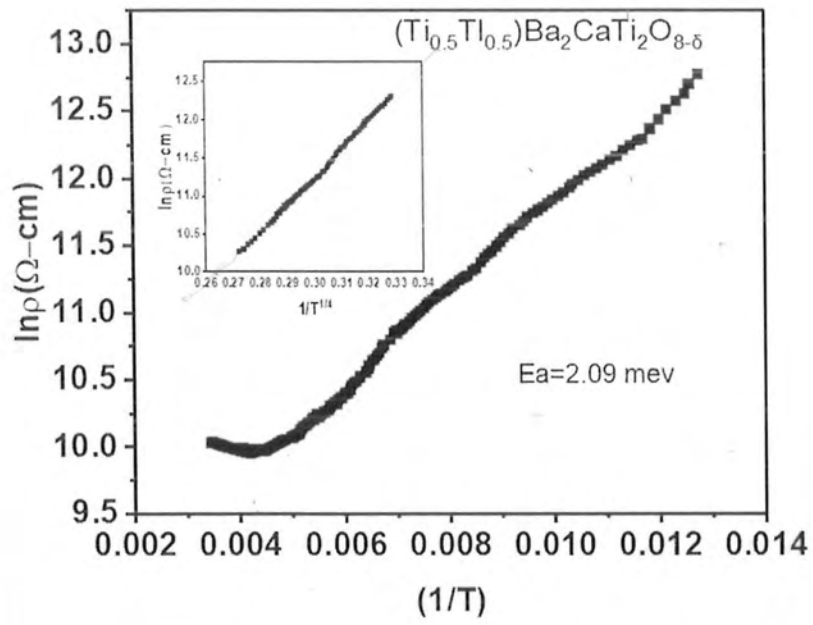


Figure 4.6 Activation energy of $\text{Ti}_{0.5}\text{Ti}_{0.5}\text{Ba}_2\text{CaTi}_2\text{O}_{8-\delta}$

4.3.3 FTIR Measurements:

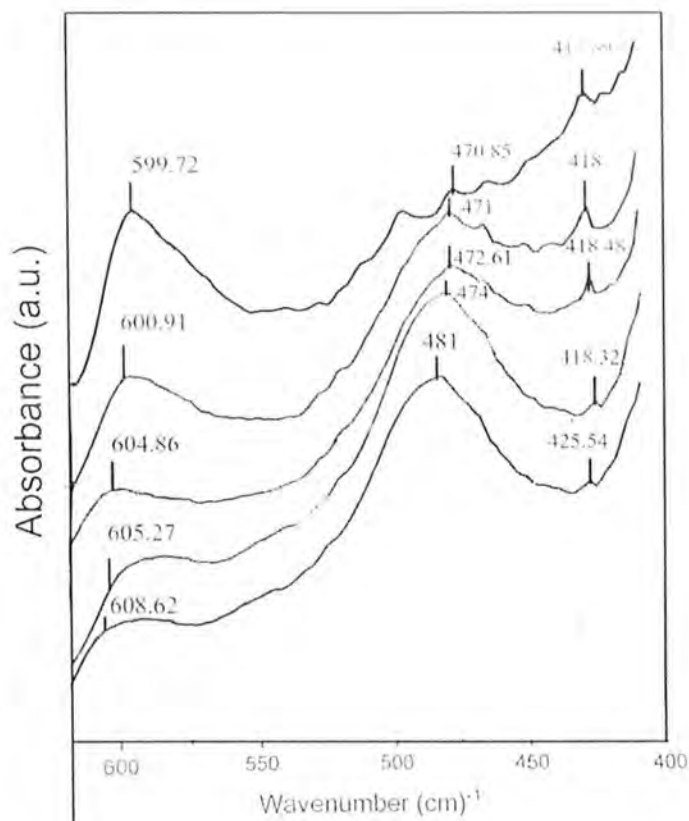


Figure 4.7 The FTIR absorption spectra of $\text{Cu}_{0.5}\text{Ti}_{0.5}\text{Ba}_2\text{CaCu}_{2-x}\text{Ti}_x\text{O}_{8-\delta}$ ($x=0, 0.5, 1, 1.5, 2.0$) samples

$\text{Cu}_{0.5}\text{Ti}_{0.5}\text{Ba}_2\text{CaCu}_{2-x}\text{Ti}_x\text{O}_{8-\delta}$ ($x=0, 0.5, 1, 1.5, 2.0$) samples' FTIR absorption data are shown in Fig. 4.7. (a,b,c,d,e). The spectrum shows three absorption bands due to the vibrations of several oxygen atoms in the unit cell, including $\text{Ti-O}_A\text{-Cu}(2)$, $\text{Cu}(1)\text{-O}_A\text{-Cu}(2)$, and a CuO_2 planar oxygen atom. These absorption bands are associated to two $\text{Ti-O}_A\text{-Cu}(2)$, $\text{Cu}(1)\text{-O}_A\text{-Cu}(2)$ planar oxygen modes that were detected around 420-480 and 480-520 cm^{-1} and 550-570 cm^{-1} , respectively. In Ti-doped materials, all three absorption bands have softened to variable degrees. All of these oxygen atoms' vibrational modes are becoming softer, which is related to the $\text{Ti}(47.9\text{amu})$ atoms' lower mass as compared to $\text{Cu}(63.546\text{amu})$. Fluctuation conductivity studies (FIC-analysis) of the conductivity data of the $\text{Cu}_{0.5}\text{Ti}_{0.5}\text{Ba}_2\text{CaCu}_{2-x}\text{Ti}_x\text{O}_{8-\delta}$ ($x=0, 0.5, 1, 1.5, 2.0$) samples have been used to examine the impact of doped atoms on the intrinsic superconducting properties of these samples.

4.3.4 $\text{Cu}_{0.5}\text{Tl}_{0.5}\text{Ba}_2\text{CaCu}_{2-x}\text{Ti}_x\text{O}_{8-\delta}$ ($x=0, 0.5, 1, 1.5, 2.0$) samples' excess conductivity analyses.

$\text{Cu}_{0.5}\text{Tl}_{0.5}\text{Ba}_2\text{CaCu}_{2-x}\text{Ti}_x\text{O}_{8-\delta}$ ($x=0, 0.5, 1, 1.5, 2.0$) samples' intrinsic superconducting properties have been examined via fluctuation conductivity analyses (FIC-analysis) of conductivity data. These analysis' results are provided below:

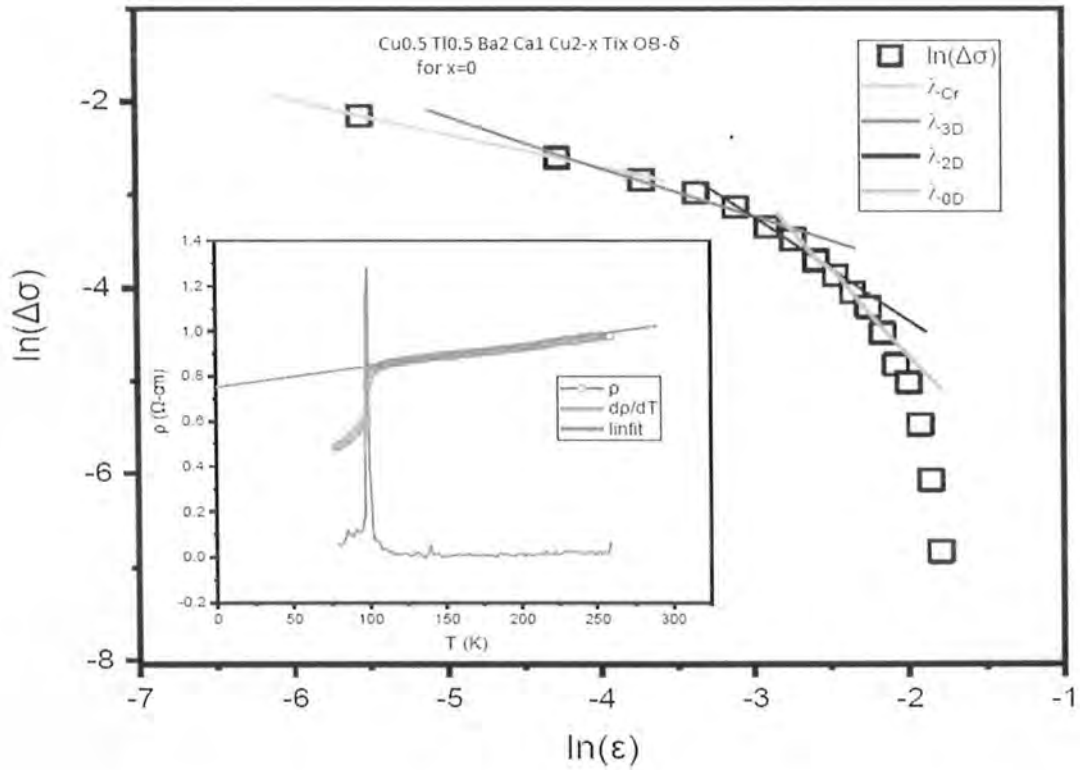


Figure 4.8 plot of $\ln(\Delta\sigma)$ and $\ln(\epsilon)$ of $\text{Cu}_{0.5}\text{Tl}_{0.5}\text{Ba}_2\text{CaCu}_{2-x}\text{Ti}_x\text{O}_{8-\delta}$ at $x=0$

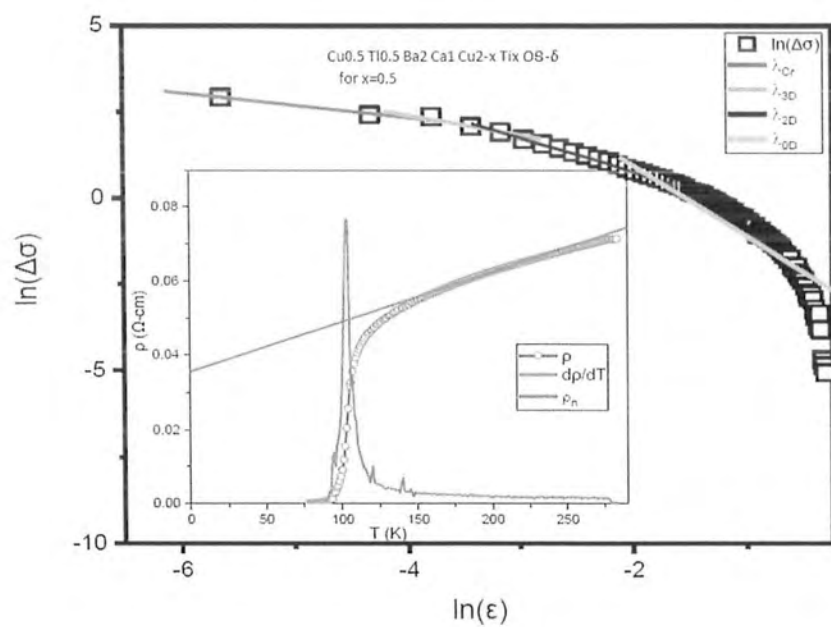


Figure 4.9 plot of $\ln(\Delta\sigma)$ and $\ln(\epsilon)$ of $\text{Cu}_{0.5}\text{Ti}_{0.5}\text{Ba}_2\text{CaCu}_{2-x}\text{Ti}_x\text{O}_{8-\delta}$ at $x=0.5$

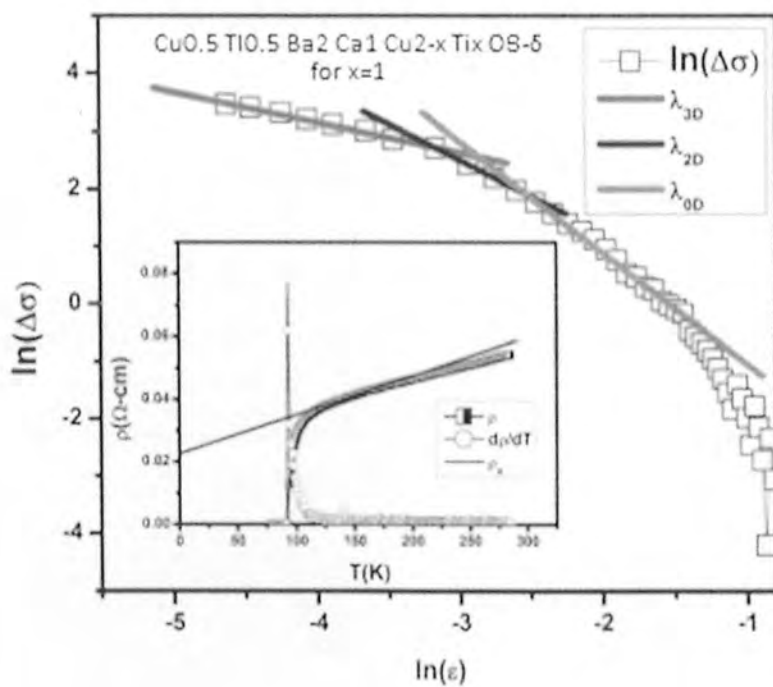


Figure 4.10 plot of $\ln(\Delta\sigma)$ and $\ln(\epsilon)$ of $\text{Cu}_{0.5}\text{Ti}_{0.5}\text{Ba}_2\text{CaCu}_{2-x}\text{Ti}_x\text{O}_{8-\delta}$ at $x=1$

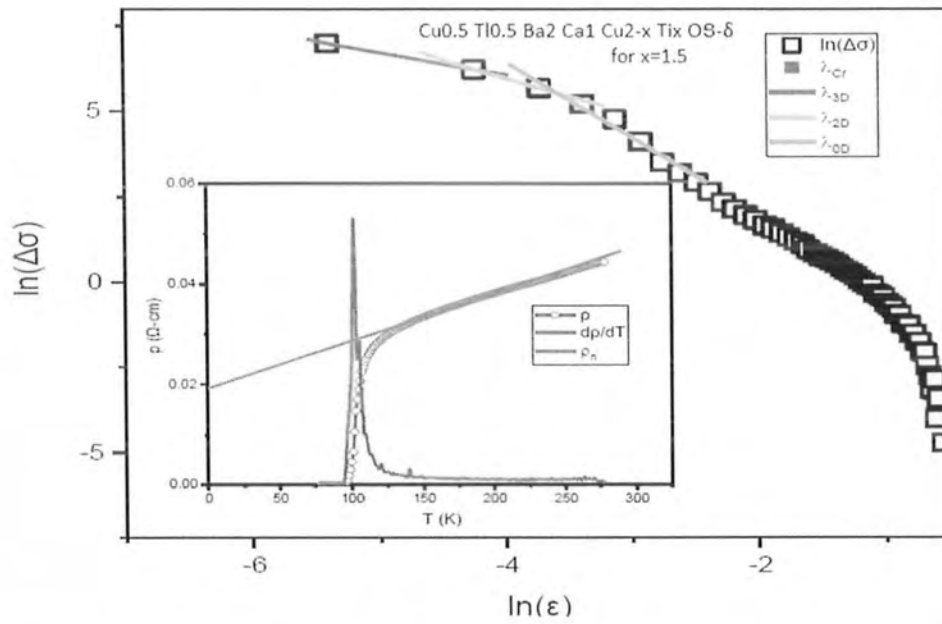


Figure 4.11 plot of $\ln(\Delta\sigma)$ and $\ln(\epsilon)$ of $\text{Cu}_{0.5}\text{Ti}_{0.5}\text{Ba}_2\text{CaCu}_{2-x}\text{Ti}_x\text{O}_{8-\delta}$ at $x=1.5$

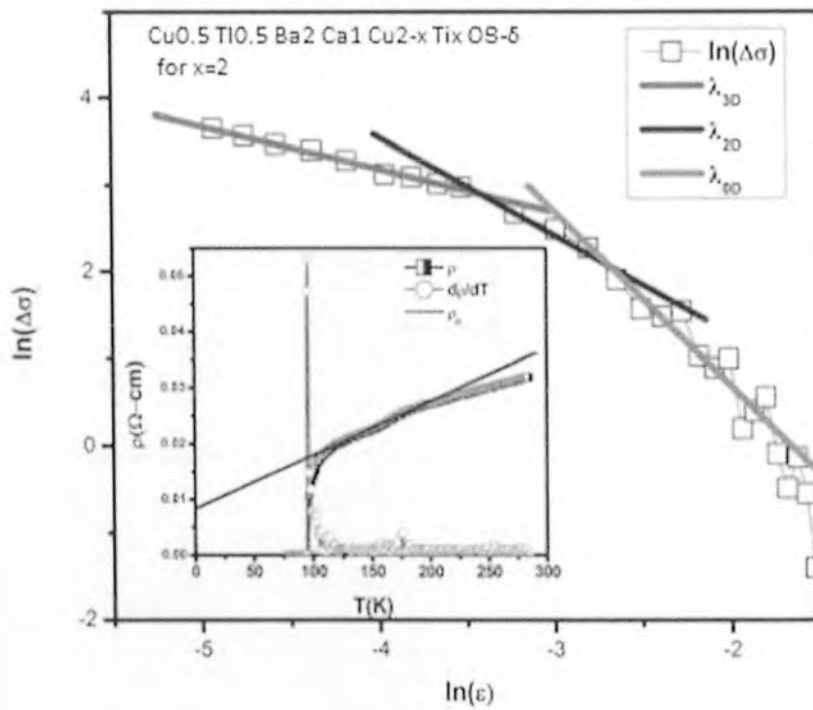


Figure 4.12 plot of $\ln(\Delta\sigma)$ and $\ln(\epsilon)$ of $\text{Cu}_{0.5}\text{Ti}_{0.5}\text{Ba}_2\text{CaCu}_{2-x}\text{Ti}_x\text{O}_{8-\delta}$ at $x=2$

The following equation is used to perform the excess conductivity studies on $\text{Cu}_{0.5}\text{Tl}_{0.5}\text{Ba}_2\text{CaCu}_{2-x}\text{Ti}_x\text{O}_{8-\delta}$ ($x=0, 0.5, 1, 1.5, 2.0$) samples.

$$\Delta\sigma_{(T)} = \Delta\sigma_{RT}\varepsilon^{-\lambda_D} \quad (4.7)$$

This equation can be written in another form by taking Log on both sides of this equation:

$$\ln \Delta\sigma_{(T)} = \ln \Delta\sigma_{RT} - \lambda_D \ln(\varepsilon) \quad (4.8)$$

Where, $\varepsilon = \left[\frac{T - T_c^{mf}}{T_c^{mf}} \right]$ = reduced temperature

λ_D = dimensional exponent.

This equation is valid for temperatures up to and including T_c . Dimensional exponent (D) values of 0.3, 0.5, 1.0, and 2.0 are related with the critical regimes of three-dimensional (3D), zero-dimensional (0D), and two-dimensional (2D) thermally activated processes, respectively. In the case of the polycrystalline samples, the expression is changed to:

$$\Delta\sigma_{LD} = [e^2 / (16 \hbar d) (1 + J\varepsilon^{-1})^{-1/2} \varepsilon^{-1}] \quad (4.9)$$

Lawrence and Doniach (LD) suggested a change to take into account the contributions from within the grains in the excess conductivity. In their formulation, $J = [2\xi_{c(0)}/d]^2$ is the coupling between the CuO_2 layers, d is the thickness of the superconducting layers (in this example, $\sim 15\text{\AA}$), and $\xi_{c(0)}$ is the coherence length along the c -axis. Using the LD-mode expression below, the coherence length is derived from the crossover temperatures.

$$\xi_{c(0)} = d/2[(T_{3D-2D}/T_{mf}) - 1]^{1/2} \quad (4.10)$$

The following equation provides the Cooper-phase pair's relaxation time:

$$\tau_{\phi} = \frac{\pi\hbar}{8k_B T \epsilon_0} \quad (4.11)$$

With the use of the phase relaxation time in the previous calculation, the coupling constant J is calculated:

$$J = \frac{\hbar \tau_{\phi}^{-1}}{2\pi k_B T} \quad (4.12)$$

The following formulas are used to determine the Fermi velocity of the carriers and the amount of energy needed to separate the Cooper pairs.

$$V_F = \frac{5\pi k_B T_c \xi_{c(0)}}{2K\hbar} \quad (4.13)$$

$$E = \frac{\hbar}{\tau_{\phi} (1.6 \times 10^{-19})} \text{ (eV)} \quad (4.14)$$

$K \cong 0.12$ is the proportionality coefficient.

TG, T3D-2D, and T2D-0D are several crossover temperatures that are the outcome of different thermally triggered processes. the intersection of several dimensional exponents, i.e., α refers to the slope below TG, 3D above TG, 2D to the slope value above T3D-2D, and 0D corresponds to the slope of exponent value 2, are used to calculate the excess conductivity vs reduced temperatures.

See Table 3

Sample	λ_{CR}	λ_{3D}	λ_{2D}	λ_{0D}	$T_{CR-3D} = T_G$ (K)	T_{3D-2D} (K)	T_{2D-0D} (K)	T_c^{mf} (K)	T^* (K)	$\alpha = \rho_n(0K)$ ($\Omega\text{-cm}$)
X=0	0.29	0.56	1.3	2	108.3737	112.387	107.40	103.05	126.053	0.0162
X=0.5	0.31	0.5	1.1	2.1	105.346	107	105.3633	102.5	136.03	2.2
X=1		0.54	1.1	1.9	102.436	105	106.4602	101.53	151.139	0.172
X=1.5		0.55	1.15	1.97	107.56	108.6	107.55	100	140	0.19
X=2		0.57	1.17	2.06	107.2	108.37	111	98	128.05	0.28

Table 3 Table of Superconducting parameters calculated from log plot of $\Delta\sigma$ and ε

The inherent superconductivity parameters for $\text{Cu}_{0.5}\text{Tl}_{0.5}\text{Ba}_2\text{CaCu}_{2-x}\text{Ti}_x\text{O}_{8-\delta}$ ($x=0, 0.5, 1, 1.5, 2.0$) samples such as $\xi_{c(0)}$, the inter-layer coupling J , V_F (the Fermi velocity) of superconducting carriers, and τ_ϕ (phase relaxation time of the carriers), are shown in table 2. The values of these parameters are marginally suppressed and decreased in comparison to un-doped samples, demonstrating that the doping of Ti in the final product has no appreciable impact on the carriers' Fermi vector, $K_F = [3\pi^2N/V]^{1/2}$.

In comparison with un-doped samples the values of such parameters are slightly suppressed decreased showing that shows that Fermi vector of the carriers $K_F = [3\pi^2N/V]^{1/2}$ is not significantly altered with the doping of Ti in the final compound; $\xi_{c(0)} = d/2[(T_{3D-2D}/T_{mf})-1]^{1/2}$.

The transition temperature between the 3D LD regime and the Ginzburg Landau (GL) regime yields the Ginzburg number, or N_G (Al-Sharabi & Abd-Shukor, 2014). The term T_G refers to this crossover temperature. The equation for and N_G can be written as follows using the T_G and T_c of a material:

$$N_G = \left| \frac{T_G - T_c}{T_c} \right| \quad (4.15)$$

The following equation is used to calculate crucial superconducting properties using NG and the Ginzbur-Landau theory.

As well as

$$N_G = 1/2[K_B T_c / B_{c(0)}^2 \gamma^2 \xi_{c(0)}^3]^2 \quad (4.16)$$

Also

$$B_{c(0)} = K_B T_c / (2N_G)^{1/2} \gamma^2 \xi_{c(0)}^3]^{1/2} \quad (4.17)$$

$$B_c = \frac{\Phi_0}{2\sqrt{2}\pi\lambda_{p,d(0)}\xi_{ab(0)}} \quad (4.18)$$

$$B_{c1} = \frac{B_c}{\kappa\sqrt{2}} \ln \kappa \quad (4.19)$$

$$B_{c2} = \sqrt{2}\kappa B_c \quad (4.20)$$

$$J_c = \frac{4\kappa B_{c1}}{3\sqrt{3}\lambda_{p,d(0)} \ln \kappa} \quad (4.21)$$

The superconductor anisotropy $\gamma = \xi_{ab(0)} / \xi_{c(0)} = 5 / (n-1)$ in this case is equal to CuTl 1212 samples with $n=2$ is $\gamma = 2.5$ and the Ginzburg Landau (GL) parameter $\kappa = \lambda / \xi$ (Al-Sharabi & Abd-

Shukor, 2014) and (Ihara et al., 1997). Here, the temperature of inflection of the resistivity temperature derivative (dp/dT) is used to calculate the mean field critical temperature (T_c^{mf}). While parameters like $\kappa=\lambda/\xi$ have increased values, parameters like $B_{c(0)}$, $J_c(0)$ have slightly lower values, indicating a decline in the number of pinning centres. In $Cu_{0.5}Tl_{0.5}Ba_2CaCu_{2-x}Ti_xO_{8-\delta}$ ($x=0, 0.5, 1, 1.5, 2.0$) samples, higher Ti doping reduces the phase relaxation time of the carriers and the energy needed to split the Cooper pairs. This demonstrates that superconducting carriers are often dispersed in Ti-doped samples and are weakly coupled, as seen in Table 4.

Samp le	$\xi_c(0)$ (Å)	J	N_G	$\lambda_{p,d} x$ 10^2 (Å)	$B_{c(0)}$ (T)	B_{c1} (T)	B_{c2} (T)	κ	$J_{c(0) x}$ 10^3 (A/cm ²)	$V_F x$ 10^7 (m/s)	E_{Break} (eV)	$\tau_{\phi} x$ 10^{-13} (s)
X=0	2.23	0.09	0.053	3.44	3.26	0.42	128	23.44	6.6	1.7	0.09	2.37
X=0.5	1.99	0.07	0.032	3.84	4.28	0.29	128	26.73	4.3	1.2	0.08	0.5
X=1	1.70	0.06	0.043	4.9	3.51	0.37	128.7	28	4.9	1.4	0.06	0.48
X=1.5	1.28	0.049	0.05	5.37	4.46	0.33	127.9	28.47	5.7	1.1	0.04	0.66
X=2	1.32	0.05	0.044	4.72	4.37	0.46	127.8	23.9	6.2	0.99	0.03	0.72

Table 4 Table of Superconducting parameters calculated from FIC

4.3.5 $Cu_{0.5}Tl_{0.5}Ba_2CaCu_{2-x}Ti_xO_{8-\delta}$ ($x=0, 0.5, 1, 1.5, 2.0$) samples' dielectric properties

Low frequencies (i.e. 78K and 100Hz) are measured for $Cu_{0.5}Tl_{0.5}Ba_2CaCu_{2-x}Ti_xO_{8-\delta}$ samples with ($x=0, 0.5, 1, 1.5, 2.0$). Higher frequencies can be applied to a material even at temperatures much below the critical temperature without causing it to become superconducting. Therefore, when measuring the dielectric properties of superconducting materials, lower frequencies are crucial. At such low frequencies, interfacial polarization predominates. Higher Ti-doping causes the real component of the dielectric constant to mostly suppress, which indicates that the samples' free carriers density is suppressed Fig.4.13. In improved Ti-doped $Cu_{0.5}Tl_{0.5}Ba_2CaCu_{2-x}Ti_xO_{8-\delta}$ ($x=0, 0.5, 1, 1.5, 2.0$) samples, the imaginary component of the dielectric constant systematically rises; dielectric loss also significantly rises in all Ti-doped samples Fig. 4.14 &

Fig. 4.15. However, all Ti-doped samples exhibit strong superconductivity and increase in ac-conductivity when compared to un-doped samples (Fig. 4.16).

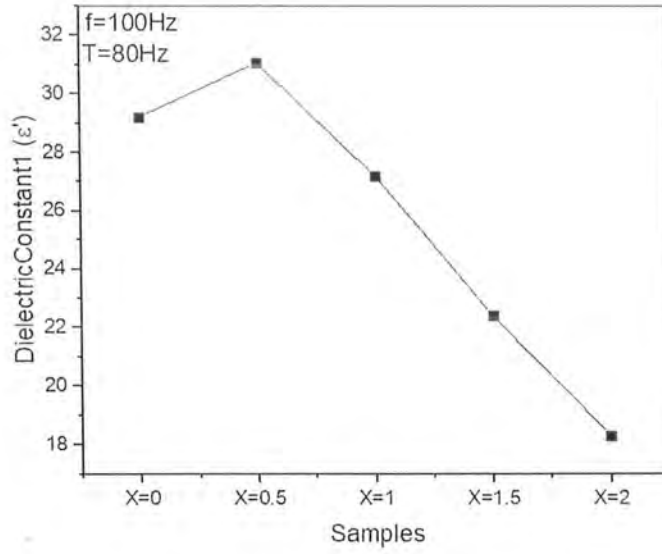


Figure 4.13 Variation of Real part of dielectric constant with increase in Ti doping measured at frequency 100Hz and temperature 78K

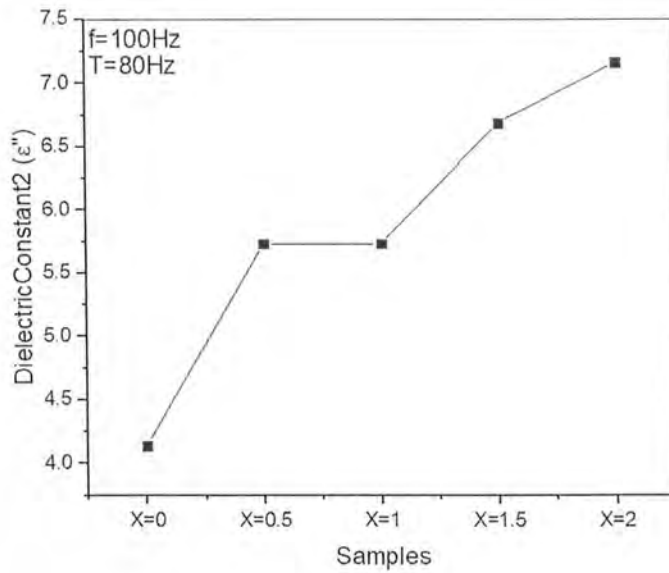


Figure 4.14 Variation of Imaginary part of dielectric constant with increase in Ti doping measured at frequency 100Hz and temperature 78K

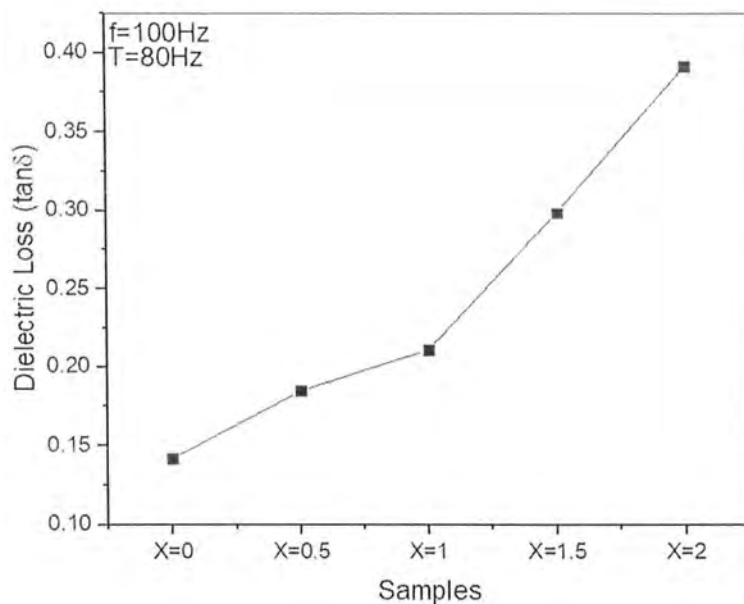


Figure 4.15 Variation of dielectric loss with increase in Ti doping measured at frequency 100Hz and temperature 78K

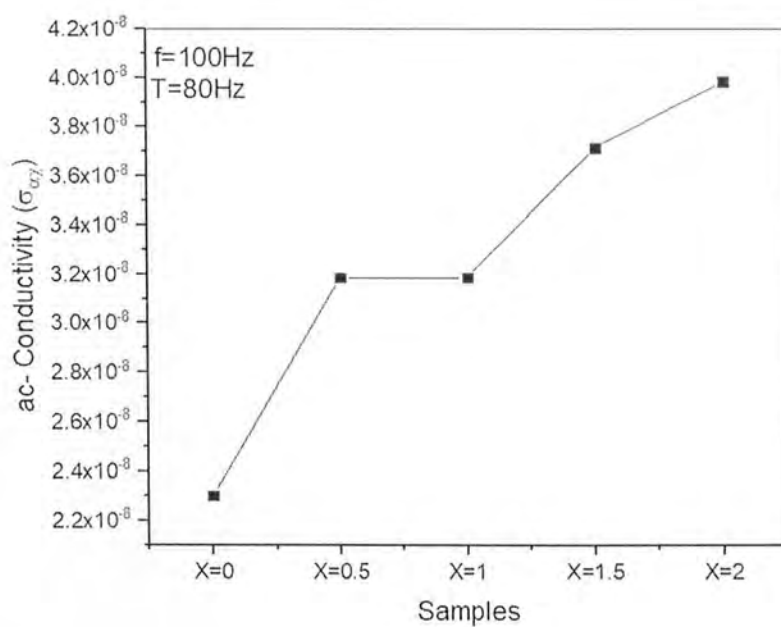


Figure 4.16 Variation of ac conductivity with increase in Ti doping measured at frequency 100Hz and temperature 80K

4.4 Conclusions:

$\text{Cu}_{0.5}\text{Tl}_{0.5}\text{Ba}_2\text{CaCu}_{2-x}\text{Ti}_x\text{O}_{8-\delta}$ ($x=0, 0.5, 1, 1.5, 2.0$) Superconductor samples are created using the solid-state reaction process, and they are assessed using measurements of their dielectric properties, resistivity, x-ray diffraction, and FTIR absorption. With the rise of Ti-doping at $x=0.5$, these samples have an orthorhombic crystal structure, and the volume of the unit cell is suppressed as Ti is added to the final compound. In the $\text{Cu}_{0.5}\text{Tl}_{0.5}\text{Ba}_2\text{CaCu}_{1.5}\text{Ti}_{0.5}\text{O}_{8-\delta}$ samples, an antiferromagnetic order is likely broken at the CuO_2 planar site, which results in an increase in the volume of the unit cell. $\text{Cu}_{0.5}\text{Tl}_{0.5}\text{Ba}_2\text{CaCu}_{2-x}\text{Ti}_x\text{O}_{8-\delta}$ ($x=0, 0.5, 1, 1.5, 2.0$) samples exhibit suppressed room temperature resistivity with increasing Ti-doping. These samples exhibit the beginning of superconductivity at temperatures of 111.3, 110.6, 112, 111.6, and 109.5 K, respectively, and the zero resistivity critical at 99, 100.3, 100, 99.8, and 100 K, respectively. Superconductivity in $\text{Cu}_{0.5}\text{Tl}_{0.5}\text{Ba}_2\text{CaTi}_2\text{O}_{8-\delta}$ is one of these samples' most notable characteristics. Due to the lower density of mobile carriers at the $\text{CuO}_2/\text{TiO}_2$ planar sites, excess conductivity analyses (FIC-analysis) of the conductivity data of these samples have revealed a slight suppression in the values of parameters like $\xi_{c(0)}$, the inter-layer coupling J , v_F (the Fermi velocity) of superconducting carriers, and the (phase relaxation time of the carriers). While parameters like $B_{c(0)}$ and $J_c(0)$ have somewhat dropped values, parameters like $\kappa=\lambda/\xi$ have increased values, indicating that the population of pinning centres in Ti-doped materials has decreased. Increased Ti-doping in the final molecule softens all of the absorption bands corresponding to the vibrations of different oxygen atoms in FTIR absorption tests. All of these oxygen atoms' vibrational modes are becoming softer, which is related to the Ti(47.9amu) atoms' lower mass as compared to Cu (63.546amu). The ac-conductivity of the dielectric constant increases in doped samples, demonstrating pronounced superconductivity in such samples, while the real part of the dielectric constant is suppressed in the dielectric measurements and the imaginary part of it increases, showing more losses in Ti-doped samples.

References

- A. A. ABRIKOSOV. (1964). *SOVIET PHYSICS JETP*. 27 April 2004.
- Al-Sharabi, A., & Abd-Shukor, R. (2014). Effect of Re substitution on the formation and fluctuation-induced conductivity of a Tl Sr₂(Ca₁-Re_x)Cu₂O_{7-δ} (x=0.05–0.30) superconductor. *Ceramics International*, 40(7), 9383–9388. <https://doi.org/10.1016/j.ceramint.2014.02.006>
- Aslamasov, L. G., & Larkin, A. I. (1968). The influence of fluctuation pairing of electrons on the conductivity of normal metal. *Physics Letters A*, 26(6), 238–239. [https://doi.org/10.1016/0375-9601\(68\)90623-3](https://doi.org/10.1016/0375-9601(68)90623-3)
- Bandyopadhyay, A. K., Varandani, D., Gmelin, E., & Narlikar, A. V. (1994). Resistivity, magnetic-susceptibility, and specific-heat studies of ErBa₂(Cu_{1-x}M_x)₃O_{7-y} [(M=Ni, Zn, Fe, Co, and Ga) and x=0.005]: The effect of site-dependent substitutional disorder. *Physical Review B*, 50(1), 462–469. <https://doi.org/10.1103/PhysRevB.50.462>
- Bardeen, J., Cooper, L. N., & Schrieffer, J. R. (1957). Microscopic Theory of Superconductivity. *Physical Review*, 106(1), 162–164. <https://doi.org/10.1103/PhysRev.106.162>
- Çavdar, Ş., Koralay, H., Tuğluoğlu, N., & Günen, A. (2005). Frequency-dependent dielectric characteristics of Tl–Ba–Ca–Cu–O bulk superconductor. *Superconductor Science and Technology*, 18(9), 1204–1209. <https://doi.org/10.1088/0953-2048/18/9/010>
- Conder, K. (2001). Oxygen diffusion in the superconductors of the YBaCuO family: isotope exchange measurements and models. *Materials Science and Engineering: R: Reports*, 32(2–3), 41–102. [https://doi.org/10.1016/S0927-796X\(00\)00030-9](https://doi.org/10.1016/S0927-796X(00)00030-9)
- Dunn, B., Chu, C., Zhou, L.-W., Cooper, J. R., & Gruner, G. (1987). PROPERTIES OF SUPERCONDUCTING OXIDES PREPARED BY THE AMORPHOUS CITRATE PROCESS. *Advanced Ceramic Materials*, 2(3B), 343–352. <https://doi.org/10.1111/j.1551-2916.1987.tb00098.x>
- F. London and H. London. (1935). The electromagnetic equations of the supraconductor. *Proceedings of the Royal Society of London. Series A - Mathematical and Physical Sciences*,

149(866), 71–88. <https://doi.org/10.1098/rspa.1935.0048>

Faix, O. (1992). *Fourier Transform Infrared Spectroscopy* (pp. 83–109). https://doi.org/10.1007/978-3-642-74065-7_7

Fossheim, K., & Sudbø, A. (2004). *Superconductivity*. John Wiley & Sons, Ltd. <https://doi.org/10.1002/0470020784>

Ginzburg, V. L., & Landau, L. D. (n.d.). On the Theory of Superconductivity. In *On Superconductivity and Superfluidity* (pp. 113–137). Springer Berlin Heidelberg. https://doi.org/10.1007/978-3-540-68008-6_4

Hagen, S. J., Jing, T. W., Wang, Z. Z., Horvath, J., & Ong, N. P. (1988). Out-of-plane conductivity in single-crystal $\text{YBa}_2\text{Cu}_3\text{O}_7$

Physical Review B, 37(13), 7928–7931. <https://doi.org/10.1103/PhysRevB.37.7928>

Handbook of Instrumental Techniques for Analytical Chemistry. (1998). *Journal of Liquid Chromatography & Related Technologies*, 21(19), 3072–3076. <https://doi.org/10.1080/10826079808006889>

Hassan, N., & Khan, N. A. (2008). Enhancement of superconducting properties in $\text{Cu}_{0.5}\text{Tl}_{0.5}\text{Ba}_2\text{Ca}_{0.5}\text{M}_{1.5}\text{Cu}_{1.5}\text{Ni}_{1.5}\text{O}_{10-\delta}$ (M=Mg, Be) superconductors. *Materials Chemistry and Physics*, 112(2), 412–416. <https://doi.org/10.1016/j.matchemphys.2008.05.074>

Hazen, R. M., Finger, L. W., Angel, R. J., Prewitt, C. T., Ross, N. L., Hadidiacos, C. G., Heaney, P. J., Veblen, D. R., Sheng, Z. Z., El Ali, A., & Hermann, A. M. (1988). 100-K superconducting phases in the Tl-Ca-Ba-Cu-O system. *Physical Review Letters*, 60(16), 1657–1660. <https://doi.org/10.1103/PhysRevLett.60.1657>

Ibach, H., & Lüth, H. (2009). *Solid-State Physics*. Springer Berlin Heidelberg. <https://doi.org/10.1007/978-3-540-93804-0>

Ihara, H., Iyo, A., Tanaka, K., Tokiwa, K., Ishida, K., Terada, N., Tokumoto, M., Sekita, Y., Tsukamoto, T., Watanabe, T., & Umeda, M. (1997). How to make superconducting-anisotropy least in high-Tc cuprate superconductors. *Physica C: Superconductivity and Its Applications*,

282–287, 1973–1974. [https://doi.org/10.1016/S0921-4534\(97\)01057-5](https://doi.org/10.1016/S0921-4534(97)01057-5)

Ihara, H., Tanaka, K., Tanaka, Y., Iyo, A., Terada, N., Tokumoto, M., Ariyama, M., Hase, I., Sundaresan, A., Hamada, N., Miyashita, S., Tokiwa, K., & Watanabe, T. (2000). Mechanism of Tc enhancement in $\text{Cu}_{1-x}\text{Tl}_x\text{-1234}$ and -1223 system with Tc \approx 130 K. *Physica C: Superconductivity*, 341–348, 487–488. [https://doi.org/10.1016/S0921-4534\(00\)00555-4](https://doi.org/10.1016/S0921-4534(00)00555-4)

Isber, S., Awad, R., Abou-Aly, A. I., Tabbal, M., & Kaouar, J. M. (2005). Electric resistivity and magnetic susceptibility studies of Tl-1223 substituted by cobalt. *Superconductor Science and Technology*, 18(3), 311–316. <https://doi.org/10.1088/0953-2048/18/3/018>

Josephson, B. D. (1962). Possible new effects in superconductive tunnelling. *Physics Letters*, 1(7), 251–253. [https://doi.org/10.1016/0031-9163\(62\)91369-0](https://doi.org/10.1016/0031-9163(62)91369-0)

Jover, D. T., Wijngaarden, R. J., Liu, R. S., Tallon, J. L., & Griessen, R. (1993). Superconductivity at 133 K in $\text{Tl}_2\text{Ba}_2\text{Ca}_2\text{Cu}_3\text{O}_{10+x}$ under high pressure. *Physica C: Superconductivity*, 218(1–2), 24–28. [https://doi.org/10.1016/0921-4534\(93\)90261-N](https://doi.org/10.1016/0921-4534(93)90261-N)

Khan, N. A., Fasih-ud-Din, & Khurram, A. A. (2005). Normal pressure synthesis of $\text{Cu}_{1-x}\text{Tl}_x\text{Ba}_2\text{Ca}_2\text{Cu}_3\text{O}_{10-\delta}$ superconductor. *Physica C: Superconductivity*, 417(3–4), 119–126. <https://doi.org/10.1016/j.physc.2004.10.012>

Khan, N. A., & Husnain, G. (2006). Superconductivity in Be substituted by Ca in $\text{Cu}_{0.5}\text{Tl}_{0.5}\text{Ba}_2\text{Ca}_{n-1-y}\text{Be}_y\text{Cu}_n\text{O}_{2n+4-\delta}$ ($n=3,4$ and $y=0.7,1.5,1.7,2.0$). *Physica C: Superconductivity*, 436(1), 51–58. <https://doi.org/10.1016/j.physc.2006.01.035>

Khan, N. A., & Khurram, A. A. (2005). Enhanced superconducting properties of $\text{Cu}_{1-x}\text{Tl}_x\text{Ba}_2\text{Ca}_2\text{-yMg}_y\text{Cu}_3\text{O}_{10-\delta}$ ($y=0, 0.5, 1.0, \text{ and } 1.5$). *Applied Physics Letters*, 86(15), 152502. <https://doi.org/10.1063/1.1899254>

Khan, N. A., & Mumtaz, M. (2006). A new $\text{Cu}_{0.5}\text{Tl}_{0.5}\text{Ba}_2\text{Ca}_2\text{Cu}_{3-y}\text{Zn}_y\text{O}_{10-\delta}$ high-temperature superconductor with three ZnO 2 planes. *Superconductor Science and Technology*, 19(8), 762–766. <https://doi.org/10.1088/0953-2048/19/8/012>

Khan, N. A., Mumtaz, M., & Khurram, A. A. (2008). Frequency dependent dielectric properties of $\text{Cu}_{0.5}\text{Tl}_{0.5}\text{Ba}_2\text{Ca}_2\text{Cu}_{3-y}\text{Zn}_y\text{O}_{10-\delta}$ ($y=0, 1.0, 1.5, 2.0, 2.5$) superconductors. *Journal of*

Applied Physics, 104(3), 033916. <https://doi.org/10.1063/1.2967823>

Khan, N. A., Saba, A., & Raza, A. (2018). Low frequency dielectric response of $\text{Cu}_{0.5}\text{Tl}_{0.5}\text{Ba}_2\text{Ca}_2\text{Cu}_3\text{-xMxO}_{10-\delta}$ (M = Cd, Zn, Ni; x=0, 1.5) superconductors. *Journal of Alloys and Compounds*, 757, 476–483. <https://doi.org/10.1016/j.jallcom.2018.02.354>

Kunzler, J. E., Buehler, E., Hsu, F. S. L., & Wernick, J. H. (1961). Superconductivity in Nb_3Sn at High Current Density in a Magnetic Field of 88 kgauss. *Physical Review Letters*, 6(3), 89–91. <https://doi.org/10.1103/PhysRevLett.6.89>

Mandal, P., Poddar, A., Das, A. N., Ghosh, B., & Choudhury, P. (1990). Excess conductivity and thermally activated dissipation studies in $\text{Bi}_2\text{Sr}_2\text{Ca}_1\text{Cu}_2\text{O}_x$ single crystals. *Physica C: Superconductivity*, 169(1–2), 43–49. [https://doi.org/10.1016/0921-4534\(90\)90287-O](https://doi.org/10.1016/0921-4534(90)90287-O)

Markovich, Robert J, C. P. (n.d.). *Introduction to Fourier Transform Infrared Spectroscopy and Applications in the Pharmaceutical Sciences*.

Marton, L.; Lark-Horovitz, K.; Johnson, V. A. (1959). *Methods of Experimental Physics: Volume 6: Solid State Physics: Part A*.

MN Rudden, J. W. (1971). *A simplified approach to solid state physics*.

Mukuda, H., Shimizu, S., Iyo, A., & Kitaoka, Y. (2012). High- T_c Superconductivity and Antiferromagnetism in Multilayered Copper Oxides –A New Paradigm of Superconducting Mechanism–. *Journal of the Physical Society of Japan*, 81(1), 011008. <https://doi.org/10.1143/JPSJ.81.011008>

Mumtaz, M., & Asghar, M. A. (2018). Dielectric properties of ferromagnetic Ni nanoparticles added ($\text{Cu}_{0.5}\text{Tl}_{0.5}\text{Ba}_2\text{Ca}_2\text{Cu}_3\text{O}_{10-\delta}$) superconducting phase. *Low Temperature Physics*, 44(8), 759–764. <https://doi.org/10.1063/1.5049155>

Muzaffar, M. U., & Khan, N. A. (2016). Effect of CuO_2 planes on the structural and superconducting transport properties of $[\text{CuTl} - 12(n - 1)n; n = 2,3,4]$ superconductor family. *International Journal of Modern Physics B*, 30(18), 1650112. <https://doi.org/10.1142/S0217979216501125>

- Nkum, R. ., Gyekye, M. ., & Boakye, F. (2002). Normal-state dielectric and transport properties of In-doped Bi–Pb–Sr–Ca–Cu–O. *Solid State Communications*, 122(10), 569–573. [https://doi.org/10.1016/S0038-1098\(02\)00159-X](https://doi.org/10.1016/S0038-1098(02)00159-X)
- Ohshima, E., Atou, T., Kikuchi, M., & Syono, Y. (1997). Stabilization of TlSr 1223 phase by high-pressure synthesis and Mo- and re-substitution for Tl. *Physica C: Superconductivity*, 282–287, 827–828. [https://doi.org/10.1016/S0921-4534\(97\)00460-7](https://doi.org/10.1016/S0921-4534(97)00460-7)
- Parkin, S. S. P., Lee, V. Y., Engler, E. M., Nazzari, A. I., Huang, T. C., Gorman, G., Savoy, R., & Beyers, R. (1988). *Bulk Superconductivity at 125 K in Tl₂Ca₂Ba₂Cu₃O_x* (pp. 309–312). https://doi.org/10.1007/978-94-011-1622-0_44
- Parkin, S. S. P., Lee, V. Y., Nazzari, A. I., Savoy, R., Beyers, R., & La Placa, S. J. (1988) Tl₁Ca_n–1Ba₂Cu_nO_{2n+3} (n=1,2,3) *Physical Review Letters*, 61(6), 750–753. <https://doi.org/10.1103/PhysRevLett.61.750>
- Rafique, M. A., Aziz, S., Hassan, N., & Khan, N. A. (2014). Enhanced Magnetic Properties in Cu_{0.5}Tl_{0.5}Ba₂Ca₂Cu₃O_{10–δ} Superconductor Doped with Carbon Nanotubes. *Journal of Superconductivity and Novel Magnetism*, 27(11), 2427–2434. <https://doi.org/10.1007/s10948-014-2617-x>
- Rahim, M., Khan, N. A., & Mumtaz, M. (2013). Temperature and Frequency Dependent Dielectric Properties of Cu_{0.5}Tl_{0.5}Ba₂Ca₃(Cu_{4–y} Cd_y)O_{12–δ} Bulk Superconductor. *Journal of Low Temperature Physics*, 172(1–2), 47–58. <https://doi.org/10.1007/s10909-012-0840-z>
- Robertson, J. H. (1986). Solid state physics by J. S. Blakemore. *Acta Crystallographica Section A Foundations of Crystallography*, 42(2), 136–136. <https://doi.org/10.1107/S0108767386099646>
- S. O.. Pillai. (2018). *Solid State Physics* (5 (Ed.)). New Academic Science., 2018. <https://www.worldcat.org/title/1129262059>
- Schmidt, V. V. (1997). *The Physics of Superconductors* (P. Müller & A. V. Ustinov (Eds.)). Springer Berlin Heidelberg. <https://doi.org/10.1007/978-3-662-03501-6>
- Sheng, Z. Z., & Hermann, A. M. (1988). Bulk superconductivity at 120 K in the Tl–Ca/Ba–Cu–O system. *Nature*, 332(6160), 138–139. <https://doi.org/10.1038/332138a0>

- Shimakawa, Y., Kubo, Y., Manako, T., & Igarashi, H. (1989). Variation in T_c and carrier concentration in Tl-based superconductors. *Physical Review B*, *40*(16), 11400–11402. <https://doi.org/10.1103/PhysRevB.40.11400>
- Simon, R., & Smith, A. (1988). *Superconductors*. Springer US. <https://doi.org/10.1007/978-1-4899-6050-4>
- Tafari, F. (Ed.). (2019). *Fundamentals and Frontiers of the Josephson Effect* (Vol. 286). Springer International Publishing. <https://doi.org/10.1007/978-3-030-20726-7>
- Tanaka, K., Iyo, A., Terada, N., Tokiwa, K., Miyashita, S., Tanaka, Y., Tsukamoto, T., Agarwal, S. K., Watanabe, T., & Ihara, H. (2001). Tl valence change and T_c enhancement ($>130\text{K}$) in $(\text{Cu,Tl})\text{Ba}_2\text{Ca}_2\text{Cu}_3\text{O}_y$ due to nitrogen annealing. *Physical Review B*, *63*(6), 064508. <https://doi.org/10.1103/PhysRevB.63.064508>
- Wu, N.-L., Yao, Y. Der, Lee, S.-N., Wong, S.-Y., & Ruckenstein, E. (1989). Synthesis of $\text{Tl}_2\text{Ca}_n\text{Ba}_2\text{Cu}_{n+1}\text{O}_{6+2n}$ ($n=1, 2$) from stoichiometric reactant mixtures. *Physica C: Superconductivity*, *161*(3), 302–312. [https://doi.org/10.1016/0921-4534\(89\)90340-7](https://doi.org/10.1016/0921-4534(89)90340-7)
- Xiao, G., Cieplak, M. Z., Gavrin, A., Streitz, F. H., Bakhshai, A., & Chien, C. L. (1988). High-temperature superconductivity in tetragonal perovskite structures: Is oxygen-vacancy order important? *Physical Review Letters*, *60*(14), 1446–1449. <https://doi.org/10.1103/PhysRevLett.60.1446>
- Younes, I., Basma, H., Anas, M., & Awad, R. (2019). Investigation of The Dielectric Properties Of (Cu, Tl) 1234 Added with Graphene. *Modern Applied Science*, *13*(4), 12. <https://doi.org/10.5539/mas.v13n4p12>

Usama Bin Ijaz Mphil Thesis

ORIGINALITY REPORT


15%	8%	12%	5%
SIMILARITY INDEX	INTERNET SOURCES	PUBLICATIONS	STUDENT PAPERS

PRIMARY SOURCES

- 1** Submitted to Higher Education Commission Pakistan
Student Paper 2%
- 2** Shafaat Hussain, Jaffar Ali, Nawazish Ali Khan, Asad Raza. "Effect of Cd intercalation on the superconducting properties of $(\text{Cu}_{0.5-y}\text{K}_{y}\text{Tl}_{1.0-y})\text{Ba}_2\text{Ca}_2\text{Cu}_{3-x}\text{Cd}_x\text{O}_{10-\delta}$ ($y = 0, 0.25$; $x = 0, 0.5, 1.0, 1.5, 2.0$) superconductors", Journal of Alloys and Compounds, 2020
Publication 1%
- 3** mafiadoc.com
Internet Source <1%
- 4** Nawazish A. Khan, Aisha Saba, Asad Raza. "Low frequency dielectric response of $\text{Cu}_{0.5}\text{Tl}_{0.5}\text{Ba}_2\text{Ca}_2\text{Cu}_{3-x}\text{M}_x\text{O}_{10-}$ ($\text{M} = \text{Cd}, \text{Zn}, \text{Ni}$; $x=0, 1.5$) superconductors", Journal of Alloys and Compounds, 2018
Publication <1%
- 5** Rehana Ahmed Abbasi, Nawazish Ali Khan, Zarmeem Malik Hafiz Sihtain Raza <1%

Usama Bin Ijaz Mphil Thesis

ORIGINALITY REPORT


19.8.2022

15%
SIMILARITY INDEX

8%
INTERNET SOURCES

12%
PUBLICATIONS

5%
STUDENT PAPERS

Professor
Department of Physics
Quaid-i-Azam University
Islamabad

PRIMARY SOURCES

- 1** Submitted to Higher Education Commission Pakistan
Student Paper **2%**
- 2** Shafaat Hussain, Jaffar Ali, Nawazish Ali Khan, Asad Raza. "Effect of Cd intercalation on the superconducting properties of $(\text{Cu}_{0.5-y}\text{K}_{y}\text{Tl}_{1.0})\text{Ba}_2\text{Ca}_2\text{Cu}_{3-x}\text{Cd}_x\text{O}_{10-\delta}$ ($y = 0, 0.25$; $x = 0, 0.5, 1.0, 1.5, 2.0$) superconductors", Journal of Alloys and Compounds, 2020
Publication **1%**
- 3** mafiadoc.com
Internet Source **<1%**
- 4** Nawazish A. Khan, Aisha Saba, Asad Raza. "Low frequency dielectric response of $\text{Cu}_{0.5}\text{Tl}_{0.5}\text{Ba}_2\text{Ca}_2\text{Cu}_{3-x}\text{M}_x\text{O}_{10}$ ($\text{M} = \text{Cd}, \text{Zn}, \text{Ni}$; $x=0, 1.5$) superconductors", Journal of Alloys and Compounds, 2018
Publication **<1%**
- 5** Rehana Ahmed Abbasi, Nawazish Ali Khan, Zarmeen Malik, Hafiz Sibtain Raza. "Superconducting properties of Ni-substituted **<1%**

CuTl-1223 superconductor", Journal of Materials Science: Materials in Electronics, 2021

Publication

6

link.springer.com

Internet Source

<1 %

7

Misbah Shafqat, Nawazish Ali Khan.

"Decoupling of CuO₂ Planes and

Superconductivity in

(Cu_{0.5}Tl_{0.5})Ba₂Ca₃Cu₄O_{12-δ}", Journal of

Superconductivity and Novel Magnetism,

2021

Publication

<1 %

8

assets.researchsquare.com

Internet Source

<1 %

9

aip.scitation.org

Internet Source

<1 %

10

moam.info

Internet Source

<1 %

11

Ş Çavdar. "Frequency-dependent dielectric characteristics of Tl-Ba-Ca-Cu-O bulk superconductor", Superconductor Science and Technology, 09/01/2005

Publication

<1 %

12

Submitted to Chester College of Higher Education

Student Paper

<1 %